JCTC Journal of Chemical Theory and Computation

pubs.acs.org/JCTC Article

Multistate Reaction Coordinate Model for Charge and Energy Transfer Dynamics in the Condensed Phase

Zengkui Liu, Haorui Hu, and Xiang Sun*

Cite This: J. Chem. Theory Comput. 2023, 19, 7151−7170 Read Online

ABSTRACT: Constructing multistate model Hamiltonians from all-atom electronic structure calculations and molecular dynamics simulations is crucial for understanding charge and energy transfer dynamics in complex condensed phases. The most popular two-level system model is the spin-boson Hamiltonian, where the nuclear degrees of freedom are represented as shifted normal modes. Recently, we proposed the general multistate nontrivial extension of the spin-boson model, i.e., the multistate harmonic (MSH) model, which is constructed by extending the spatial dimensions of each nuclear mode so as to satisfy the all-atom reorganization energy restrictions for all pairs of electronic states.

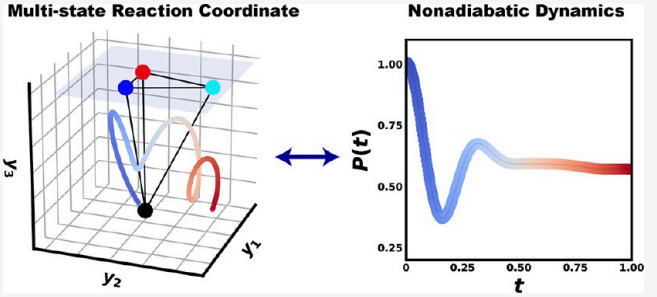

In this work, we propose the multistate reaction coordinate (MRC) model with a primary reaction coordinate and secondary bath modes as in the Caldeira-Leggett form but in extended spatial dimensions. The MRC model is proven to be equivalent to the MSH model and offers an intuitive physical picture of the nuclear-electronic feedback in nonadiabatic processes such as the inherent trajectory of the reaction coordinate. The reaction coordinate is represented in extended dimensions, carrying the entire reorganization energies and bilinearly coupled to the secondary bath modes. We demonstrate the MRC model construction for photoinduced charge transfer in an organic photovoltaic caroteniod-porphyrin-C_{60} molecular triad dissolved in tetrahydrofuran as well as excitation energy transfer in a photosynthetic light-harvesting Fenna-Matthews-Olson complex. The MRC model provides an effective and robust platform for investigating quantum dissipative dynamics in complex condensed-phase systems since it allows a consistent description of realistic spectral density, state-dependent system-bath couplings, and heterogeneous environments due to static disorder in reorganization energies.

1. INTRODUCTION

Photoinduced energy conversion inevitably involves quantum transitions between multiple electronic states, for instance, photoinduced charge transfer (CT) and excitation energy transfer (EET) in photovoltaic cells, organic electronics, and photosynthetic light-harvesting complexes.[1−16] Theoretical calculations for such processes can help to elucidate the key factors that contribute to the efficiency and pathways of energy conversion. The microscopic mechanisms of charge and energy transport dynamics has a nonadiabatic nature, where the Born−Oppenheimer approximation of separating electronic and nuclear degrees of freedom (DOF) breaks down.[17−20] Theoretical understanding of such processes requires suitable dynamic theories as well as effective Hamiltonians.

In recent years, many quantum dynamical methods were developed to simulate the "numerically" exact charge and energy transfer dynamics, including real-time path integral approaches,[21,22] hierarchical equations of motion (HEOM),[23,24] and wave function-based multiconfiguration time-dependent Hartree (MCTDH),[25−27] time-dependent density matrix renormalization group (TD-DMRG),[28−30] and tensor-train thermofield dynamics (TT-TFD),[31,32] to name a few. These methods could only treat simple low-dimensional systems such as single molecules or model Hamiltonians because the computational cost increases drastically with the system size. On the other hand, approximate nonadiabatic dynamical methods have found a much larger application scope ranging from complex molecular to condensed-phase systems, such as mixed quantum-classical,[17−20] quasiclassical,[33−36] and semiclassical[37−39] methods.

For condensed-phase systems, it is desirable to simulate the nonadiabatic dynamics with all-atom details, but the prohibitively large dimensionality makes this task difficult. Using an effective model Hamiltonian offers a very attainable and straightforward computational alternative to the problem. A common strategy is to propose a form of model Hamiltonian whose parameters are either assumed or deduced from experiments or calculations.[40−47] For example, one of the

Received: July 13, 2023
Published: October 10, 2023

https://doi.org/10.1021/acs.jctc.3c00770
J. Chem. Theory Comput. 2023, 19, 7151−7170

best approaches is to construct effective models by mapping from the all-atom anharmonic Hamiltonian with the help of electronic structure calculations and molecular dynamics simulations.[44−47]

The most popular model for charge and energy transfer in a two-level system is the spin-boson Hamiltonian, which has been applied to study many quantum dissipative dynamics.[46−49] In spin-boson Hamiltonian, the nuclear DOF are represented as a collection of shifted normal modes, which are bilinearly coupled to the electronic DOF. The harmonic normal mode approximation works rather well in the condensed phases due to a large number of molecules and the central limit theorem in contrast to the situation in a single molecule where some relevant torsional motion may not be well described by a harmonic potential. Denoting the two electronic states as the donor state $|D\rangle$ and the acceptor state $|A\rangle$, we can express the spin-boson Hamiltonian as

$$\hat{H}_{\mathrm{SB}} = \varepsilon\hat{\sigma}_z + \Gamma_{DA}\hat{\sigma}_x + \sum_{j=1}^{N}\left(\frac{\hat{P}_j^2}{2} + \frac{1}{2}\tilde{\omega}_j^2\hat{R}_j^2 - \tilde{c}_j\hat{R}_j\hat{\sigma}_z\right) \tag{1}$$

where $\hat{\sigma}_z = |D\rangle\langle D| - |A\rangle\langle A|$ and $\hat{\sigma}_x = |D\rangle\langle A| + |A\rangle\langle D|$ are the electronic Pauli matrices; Γ_{DA} is the electronic coupling; $-\Delta E = 2\varepsilon = \hbar\omega_{DA}$ is the donor-to-acceptor reaction free energy. In addition, $\{\hat{R}_j, \hat{P}_j, \tilde{\omega}_j | j = 1, ..., N\}$ are the mass-weighted coordinates, momenta, and frequencies of the N nuclear normal modes, respectively, and $\{\tilde{c}_j\}$ are the electronic-nuclear coupling coefficients. The parameter values for $\{\tilde{\omega}_j, \tilde{c}_j\}$ can be determined by the spectral density defined as

$$J(\omega) = \frac{\pi}{2}\sum_{j=1}^{N}\frac{\tilde{c}_j^2}{\tilde{\omega}_j}\delta(\omega - \tilde{\omega}_j) \tag{2}$$

The spectral density sometimes is assumed to be certain analytical forms such as Ohmic and Debye types[40,41,49,50] or can be obtained from realistic all-atom simulations using its direct relation with the time correlation function (TCF) of the energy gap between two electronic states.[44−47] The reorganization energy between the two states is proportional to the variance of their energy gap and also related to the spectral density integral:

$$E_r = \frac{4}{\pi}\int_0^\infty \frac{J(\omega)}{\omega}\,\mathrm{d}\omega = \frac{\sigma_{DA}^2}{2k_{\mathrm{B}}T} \tag{3}$$

where $\sigma_{DA}^2 = \langle U_{DA}^2\rangle - \langle U_{DA}\rangle^2$ and $U_{DA} = V_D - V_A$ is the donor−acceptor energy gap.

However, when one goes beyond the two-state scenario, proposing an effective model Hamiltonian that is consistent with all-atom Hamiltonian becomes more challenging because the number of reorganization energies is not equal to the number of electronic states.[51,52] In a general F-state system, the fundamental problem is that there are $C_F^2 = F(F-1)/2$ pairs of energy gaps and thus $F(F-1)/2$ reorganization energy restrictions, which is more than the number of states. In the traditional isolated bath models such as the Frenkel exciton model, as shown in Figure 1(a), each excited state is connected to its own bath characterized by the reorganization energy between this excited state and the ground state (the local bath), and there is no communication between the baths belonging to different excited states. Essentially, the isolated bath model could use only F excited-/ground-state reorganization energy restrictions from all-atom simulations.

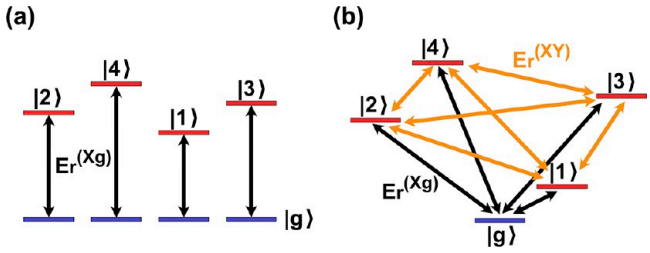

Figure 1. Comparison of traditional isolated bath models (a) such as the Frenkel exciton model with reorganization energy restrictions only between excited states and their own local bath ground states (black) versus our multistate harmonic (MSH) or multistate reaction coordinate (MRC) models (b) with reorganization energy restrictions between all possible pairs of states including excited state-excited state correlations (orange).

Recently, we proposed a consistent way to incorporate all reorganization energies in the multistate harmonic (MSH) Hamiltonian.[53] The idea is that one needs to extend the spatial dimension of each normal mode from 1 to $F-1$ in order to simultaneously satisfy the $F(F-1)/2$ reorganization energy restrictions from all-atom simulations. As shown in Figure 1(b), the ground state and all excited states are treated on an equal footing, and the communications between all pairs of states are accounted for in terms of the reorganization energies. Effectively, the locations of the potential energy surface (PES) minima of all F states can be represented by vertices of a polyhedron in $F-1$-dimensional space, whose edge lengths are proportional to the square roots of the corresponding reorganization energies.[53] Incorporating the reorganization energy restrictions between excited states is important. For example, it has been demonstrated that the MSH model provides accurate nonadiabatic dynamics compared with all-atom nonadiabatic semiclassical dynamics in a prototypical photoinduced CT process involving a carotenoid-porphyrin-C_{60} (CPC_{60}) triad dissolved in explicit tetrahydrofuran solvent.[54] In the meanwhile, the isolated bath model gives rise to significant deviations in nonadiabatic dynamics from the reference, which can be ascribed to the lack of explicit treatment for the correlations between all excited states.[53] The globally shared bath in the MSH model mimics one or more chemical species on different electronic states immersed in a correlated and heterogeneous environment, and it can also describe the case when some or all electronic states have uncorrelated bath modes, which is represented as orthogonal PES minima, if that is what all-atom simulations dictate. The MSH model's ability to account for the heterogeneous environment for multiple electronic states, either on the same molecule or belonging to different molecules, makes it a general and consistent Hamiltonian for charge and energy transfer dynamics in complex condensed phases.[55]

Despite the straightforwardness of the MSH model, the collective and delocalized normal modes still lack a clear physical picture to answer which nuclear motion really pushes the reaction forward. A reaction coordinate (RC), if any, provides a clear physical picture of nonadiabatic dynamics, such as an intuitive measure of the reaction progress in terms of the current nuclear distribution and the characteristic time scale of the RC. Searching for the RC of chemical reactions has a long history. Particularly in quantum dynamics, the Caldeira-

https://doi.org/10.1021/acs.jctc.3c00770
J. Chem. Theory Comput. 2023, 19, 7151−7170

Leggett (CL) Hamiltonian has been used widely in quantum dissipative systems and superconducting quantum-interference devices (SQUID).[56−58] Garg, Onuchic, and Ambegaokar applied the CL-type of Hamiltonian with a harmonic reaction coordinate to the two-state electron transfer problem.[59] Burghardt and co-workers extended the spin-boson model to an effective-mode Hamiltonian, which represents the vibrational modes in terms of a series of effective modes while the rest of the bath modes are truncated as approximate spectral densities in order to reduce the bath dimensionality and computational cost.[60−62] Recently, Popp et al. reported Frenkel and CT exciton dynamics in oligothiophene aggregates using a reduced-dimensional effective-mode model.[63−65] Makri proposed a system-bath Hamiltonian in extended dimensions, where the reorganization energies and the PES minima between any pair of sites are identical and independent of site-to-site distance.[66] However, there is still no clear way to map a heterogeneous and globally shared bath for multiple electronic states such as in MSH model to a well-defined reaction coordinate, which is coupled to a secondary bath.

In this work, we propose a systematic way to transform the MSH model defined in the normal mode basis into the multistate reaction coordinate (MRC) model, where the electronic subspace is coupled only to the RC, and the RC is coupled to the secondary bath modes. The main purpose is to find the MRC Hamiltonian that is exactly equivalent to the MSH Hamiltonian rather than an approximate way. We will test the equivalence between the MRC and the MSH models in two prototypical systems, including the photoinduced CT in the CPC_{60} triad dissolved in explicit solvent[67−71] and the EET in photosynthetic light-harvesting Fenna−Matthews−Olson (FMO) complex.[40,41,44,45,55,72−76] We employ several nonadiabatic semiclassical dynamics methods, but our focus here is whether the two models using the same dynamical methods give rise to identical results rather than comparing the accuracy between different dynamical methods. A benefit of RC is that one can easily prepare a nonequilibrium initial nuclear state with predefined shifts with respect to all electronic states.

The remainder of this work is organized as follows. Section 2 presents the construction of the MRC model Hamiltonian by building up from the single-state CL model, the two-state Garg-Onuchic-Ambegaokar (GOA) model, and the MSH model. Section 3 provides simulation details for constructing MRC models for the photoinduced CT in the CPC_{60} triad dissolved in organic solvent as well as EET in photosynthetic light-harvesting FMO complex in *Chlorobaculum tepidum* (*C. tepidum*) and *Prosthecochloris aestuarii* (*P. aestuarii*). Section 4 presents the results and discussion. Section 5 provides the concluding remarks. Appendix A provides the formulas for the equilibrium shifts in the MRC and MSH models.

2. MODEL HAMILTONIANS

2.1. Single-State Caldeira-Leggett Model. The simplest reaction coordinate model is the single-state Caldeira−Leggett (CL) Hamiltonian,[56,57] which is composed of a primary reaction coordinate, $\hat{y}$, subject to an arbitrary potential $V_0(\hat{y})$ that can be harmonic or anharmonic, and a collection of secondary harmonic bath modes, $\{\hat{x}_\alpha|\alpha = 1, ..., N-1\}$, and the primary mode and the secondary bath modes are bilinearly coupled:

$$\hat{H}_{\mathrm{CL}} = \frac{\hat{p}_y^2}{2} + V_0(\hat{y}) + \sum_{\alpha=1}^{N-1}\left[\frac{\hat{p}_\alpha^2}{2} + \frac{1}{2}\omega_\alpha^2\left(\hat{x}_\alpha + \frac{c_\alpha}{\omega_\alpha^2}\hat{y}\right)^2\right] \tag{4}$$

2.2. Two-State Garg-Onuchic-Ambegaokar Model. The Garg-Onuchic-Ambegaokar (GOA) model was proposed for two electronic states, where the primary/secondary mode representation of the CL Hamiltonian is adopted for each state, and the PES of the primary mode on two states is assumed to be a shifted harmonic potential.[58,59] The advantage of the GOA model over the spin-boson model is a clear physical picture provided by the reaction coordinate. The GOA Hamiltonian is given by

$$\hat{H}_{\mathrm{GOA}} = \varepsilon\hat{\sigma}_z + \Gamma_{DA}\hat{\sigma}_x + \frac{\hat{p}_y^2}{2} + \frac{1}{2}\Omega^2(y + y_0\hat{\sigma}_z)^2 + \sum_{\alpha=1}^{N-1}\left[\frac{\hat{p}_\alpha^2}{2} + \frac{1}{2}\omega_\alpha^2\left(\hat{x}_\alpha + \frac{c_\alpha}{\omega_\alpha^2}\hat{y}\right)^2\right] \tag{5}$$

Here, $\hat{y}$, $\hat{P}_y$, and Ω are the primary reaction coordinate's mass-weighted coordinate, momentum, and frequency, respectively; $\{\hat{x}_\alpha, \hat{p}_\alpha, \omega_\alpha|\alpha = 1, ..., N-1\}$ are the mass-weighted coordinates, momenta, and frequencies of the secondary bath modes, respectively; $\{c_\alpha\}$ is the coupling coefficients between the primary mode and the secondary modes, which should be discerned from the electronic-nuclear couplings $\{\tilde{c}_j\}$ for all normal modes in the spin-boson model; $2y_0$ is the distance in equilibrium geometries of the primary mode between the two states, such that the reorganization energy is absorbed entirely to the primary mode, i.e.,

$$E_r = 2\Omega^2 y_0^2 \tag{6}$$

In the original GOA model, the secondary bath is assumed to follow the Ohmic spectral density given by

$$J_{\mathrm{bath}}(\omega) = \frac{\pi}{2}\sum_{\alpha=1}^{N-1}\frac{c_\alpha^2}{\omega_\alpha}\delta(\omega - \omega_\alpha) \to J_{\mathrm{Ohm}}(\omega) = \eta\omega\, \mathrm{e}^{-\omega/\omega_c} \tag{7}$$

where η is the friction coefficient and ω_c is the cutoff frequency. It is worth noting that an asymptotic effective spectral density for the corresponding normal modes in eq 2 was derived for the specific Ohmic bath spectral density at the limit $\Omega \ll \omega_c$ by GOA[59]

$$J_{\mathrm{eff}}^{(1)}(\omega) = \frac{\eta\omega\Omega^4 y_0^2}{(\Omega^2 - \omega^2)^2 + \eta^2\omega^2} \tag{8}$$

following the Leggett prescription:[57]

$$J_{\mathrm{eff}}(\omega) = \lim_{\varepsilon\to 0^+}\mathrm{Im}[K(\omega - i\varepsilon)],\ (\omega, \varepsilon \text{ are real}) \tag{9}$$

where with complex z and real ω',

$$K(z) = -z^2 + \Omega^2 y_0^2\frac{L(z)}{L(z) + \Omega^2} \tag{10}$$

$$L(z) = -z^2\left[1 + \frac{2}{\pi}\int_0^\infty \mathrm{d}\omega'\frac{J_{\mathrm{Ohm}}(\omega')}{\omega'(\omega'^2 - z^2)}\right] \tag{11}$$

https://doi.org/10.1021/acs.jctc.3c00770
J. Chem. Theory Comput. 2023, 19, 7151−7170

However, the effective spectral density $J_{\text{eff}}^{(1)}(\omega)$ in some parameter regions such as $\Omega \sim \omega_c$ could be inaccurate. For example, there can be significant deviation in Fermi's golden rule rate constant between the spin-boson model with numerically accurate discrete normal modes (eq 2) and the effective spectral density (eq 8),[77] so caution is advised.

The GOA model and spin-boson model are equivalent and can be transformed from one to the other. To transform from the GOA model to the spin-boson model, one diagonalizes the Hessian matrix of the GOA potential energy surface of either state given by

$$\mathbf{D} = \begin{pmatrix} \Omega^2 + \sum_\alpha \frac{c_\alpha^2}{\omega_\alpha^2} & c_1 & c_2 & \cdots & c_{N-1} \\ c_1 & \omega_1^2 & & & \\ c_2 & & \omega_2^2 & & \\ \vdots & & & \ddots & \\ c_{N-1} & & & & \omega_{N-1}^2 \end{pmatrix} \tag{12}$$

such that

$$\mathbf{T}^T\mathbf{D}\mathbf{T} = \text{diag}(\tilde{\omega}_1^2, ..., \tilde{\omega}_N^2) \tag{13}$$

giving rise to N normal-mode frequencies $\{\tilde{\omega}_j | j = 1, ..., N\}$. The spin-boson model can also be expressed in terms of the donor-to-acceptor distance in equilibrium geometry along the normal mode coordinates or $\{R_j^{\text{eq}}\}$:[78]

$$\begin{aligned} \hat{H}_{\text{SB}} &= \hat{H}_D|D\rangle\langle D| + \hat{H}_A|A\rangle\langle A| + \Gamma_{DA}(|D\rangle\langle A| + |A\rangle\langle D|), \\ \hat{H}_D &= \sum_{j=1}^N \frac{\hat{P}_j^2}{2} + \frac{1}{2}\sum_{j=1}^N \tilde{\omega}_j^2 \hat{R}_j^2 + \varepsilon, \\ \hat{H}_A &= \sum_{j=1}^N \frac{\hat{P}_j^2}{2} + \frac{1}{2}\sum_{j=1}^N \tilde{\omega}_j^2 (\hat{R}_j - R_j^{\text{eq}})^2 - \varepsilon \end{aligned} \tag{14}$$

and the equilibrium geometry distances $\{R_j^{\text{eq}}\}$ are given by

$$\begin{pmatrix} R_1^{\text{eq}} \\ R_2^{\text{eq}} \\ \vdots \\ R_N^{\text{eq}} \end{pmatrix} = 2y_0 \mathbf{T}^T \begin{pmatrix} 1 \\ -\frac{c_1}{\omega_1^2} \\ \vdots \\ -\frac{c_{N-1}}{\omega_{N-1}^2} \end{pmatrix} \tag{15}$$

The reorganization energy is given by

$$E_r = \sum_{j=1}^N \frac{1}{2}\tilde{\omega}_j^2 (R_j^{\text{eq}})^2 \tag{16}$$

Comparing eq 14 with eq 1, we have the relation $R_j^{\text{eq}} = 2\tilde{c}_j/\tilde{\omega}_j^2$, $(j = 1, ..., N)$.

To construct the spin-boson model parameters $\{\tilde{\omega}_j, \tilde{c}_j\}$ for any two states X, Y (without loosing generality) from all-atom molecular dynamics (MD) simulations, one could use the energy-gap time correlation function (TCF) as an input:

$$C_{UU}^{(XY)}(t) = \langle U_{XY}(t)U_{XY}(0)\rangle - \langle U_{XY}\rangle^2 \tag{17}$$

where $U_{XY} = V_X - V_Y$ is the energy gap between state X and Y. The spectral density is related to the energy-gap TCF via[46,47,52,53]

$$J^{(XY)}(\omega) = \frac{\beta\omega}{4}\int_0^\infty \mathrm{d}t\ C_{UU}^{(XY)}(t)\cos(\omega t) \tag{18}$$

The reorganization energy between states X and Y, E_r, scales with the TCF at time 0, $C_{UU}^{(XY)}(0) = \sigma_{XY}^2 = \langle U_{XY}^2\rangle - \langle U_{XY}\rangle^2$:

$$E_r^{(XY)} = \frac{C_{UU}^{(XY)}(0)}{2k_{\text{B}}T} \tag{19}$$

One can determine the frequencies $\{\tilde{\omega}_j\}$ and the electronic-nuclear coupling coefficients $\{\tilde{c}_j\}$ or equivalently the equilibrium geometry distances $\{R_j^{(XY)}\}$ by discretizing the spectral density $J^{(XY)}(\omega)$. The discretization into N modes is achieved by solving the following equation for $\tilde{\omega}_j (j = 1,2, ..., N)$:

$$\frac{2N\tilde{\omega}_j}{\pi C_{UU}^{(XY)}(0)}\int_0^\infty \mathrm{d}t\ \frac{C_{UU}^{(XY)}(t)}{\tilde{\omega}_j t}\sin(\tilde{\omega}_j t) = j - \frac{1}{2} \tag{20}$$

The corresponding system-bath coupling coefficients, c_j, and the equilibrium geometry distances, $R_j^{(XY)}$, are given by

$$\tilde{c}_j = \sqrt{\frac{E_r^{(XY)}}{2N}}\,\tilde{\omega}_j \tag{21}$$

$$R_j^{(XY)} = \frac{2\tilde{c}_j}{\tilde{\omega}_j^2} = \sqrt{\frac{2E_r^{(XY)}}{N}}\frac{1}{\tilde{\omega}_j} = a_j\sqrt{E_r^{(XY)}} \tag{22}$$

where

$$a_j = \sqrt{\frac{2}{N}}\frac{1}{\tilde{\omega}_j}\ (j = 1,2, ..., N) \tag{23}$$

In this way, each mode contributes to the overall reorganization energy equally and the reorganization energy is given by

$$E_r^{(XY)} = \sum_{j=1}^N \frac{1}{2}\tilde{\omega}_j^2 (R_j^{(XY)})^2 = \sum_{j=1}^N \frac{2\tilde{c}_j^2}{\tilde{\omega}_j^2} \tag{24}$$

2.3. Multistate Harmonic Model. Now we consider a general F-state Hamiltonian that is given by

$$\hat{H} = \begin{pmatrix} \hat{H}_1 & \hat{\Gamma}_{12} & \hat{\Gamma}_{13} & \cdots & \hat{\Gamma}_{1F} \\ \hat{\Gamma}_{21} & \hat{H}_2 & \hat{\Gamma}_{23} & \cdots & \hat{\Gamma}_{2F} \\ \hat{\Gamma}_{31} & \hat{\Gamma}_{32} & \hat{H}_3 & \cdots & \hat{\Gamma}_{3F} \\ \vdots & \vdots & \vdots & \ddots & \vdots \\ \hat{\Gamma}_{F1} & \hat{\Gamma}_{F2} & \hat{\Gamma}_{F3} & \cdots & \hat{H}_F \end{pmatrix} \tag{25}$$

where the nuclear Hamiltonians of the F states in MSH model proposed in ref 53 are given by

https://doi.org/10.1021/acs.jctc.3c00770
J. Chem. Theory Comput. 2023, 19, 7151−7170

$$\hat{H}_1 = \sum_{i=1}^{F-1}\sum_{j=1}^{N}\frac{\hat{P}_{i,j}^2}{2} + \sum_{j=1}^{N}\frac{1}{2}\tilde{\omega}_j^2[\hat{R}_{1,j}^2 + \hat{R}_{2,j}^2 + \cdots + \hat{R}_{F-1,j}^2] + \varepsilon_1,$$

$$\hat{H}_2 = \sum_{i=1}^{F-1}\sum_{j=1}^{N}\frac{\hat{P}_{i,j}^2}{2} + \sum_{j=1}^{N}\frac{1}{2}\tilde{\omega}_j^2[(\hat{R}_{1,j} - S_j^{(12)})^2 + \hat{R}_{2,j}^2 + \cdots + \hat{R}_{F-1,j}^2] + \varepsilon_2,$$

$$\hat{H}_3 = \sum_{i=1}^{F-1}\sum_{j=1}^{N}\frac{\hat{P}_{i,j}^2}{2} + \sum_{j=1}^{N}\frac{1}{2}\tilde{\omega}_j^2[(\hat{R}_{1,j} - S_j^{(13)})^2 + (\hat{R}_{2,j} - S_j^{(23)})^2 + \cdots + \hat{R}_{F-1,j}^2] + \varepsilon_3,$$

$$\cdots$$

$$\hat{H}_F = \sum_{i=1}^{F-1}\sum_{j=1}^{N}\frac{\hat{P}_{i,j}^2}{2} + \sum_{j=1}^{N}\frac{1}{2}\tilde{\omega}_j^2[(\hat{R}_{1,j} - S_j^{(1F)})^2 + (\hat{R}_{2,j} - S_j^{(2F)})^2 + \cdots + (\hat{R}_{F-1,j} - S_j^{(F-1,F)})^2] + \varepsilon_F \tag{26}$$

Here, $\{\tilde{\omega}_j | j = 1, ..., N\}$ are the N physical normal-mode frequencies, which can be obtained similarly as the two-state case using eq 20; the index $i = 1, ..., F-1$ labels the $F-1$ extended subspaces of the physical normal modes resulting in the total nuclear DOF $N_n = (F-1) \times N$; $\{S_j^{(XY)} | 1 \le X < Y \le F\}$ are the equilibrium (horizontal) shift components for the PES of state Y along the j-th mode; $\{\varepsilon_X | X = 1, ..., F\}$ are the energy minima (vertical shifts) of the PESs of the different electronic states; $\{\hat{\Gamma}_{XY} | X, Y \in (1, ..., F), X \ne Y\}$ are the electronic couplings and $\hat{\Gamma}_{XY} = \Gamma_{XY}$ is constant under the Condon approximation.

As detailed in ref 53, we introduced the general way for constructing the MSH model Hamiltonian from multistate all-atom MD simulations and quantum chemistry calculations. In short, one needs excited-state electronic structure calculations to determine the excitation energy and the charge distribution for each electronic state, and MD simulations to determine $F(F-1)/2$ energy-gap TCFs between all possible pairs of states, namely $\{C_{UU}^{(XY)}(t) | X < Y\}$. From these energy-gap TCFs, we can compute all of the reorganization energies using eq 19.

As an important feature of the MSH model, the dimensionality of each normal mode is extended from 1 to $F-1$ such that the equilibrium positions of all F electronic states form a polyhedron with F vertices, and the equilibrium distances between any pair of states satisfy the reorganization energy restrictions in eq 22. In particular, the $F(F-1)/2$ sets of equilibrium shifts

$$\{S_j^{(12)}, S_j^{(13)}, S_j^{(23)}, ..., S_j^{(F-1,F)}\} \tag{27}$$

need to satisfy the $F(F-1)/2$ reorganization energy restrictions that require the equilibrium geometry distances (the polyhedron edges) between each pair of states proportional to

$$\sqrt{E_r^{(12)}}, \sqrt{E_r^{(13)}}, \sqrt{E_r^{(23)}}, ..., \sqrt{E_r^{(F-1,F)}} \tag{28}$$

In this way, we can achieve a consistent account for all of the reorganization energies between $F(F-1)$ pairs of states obtained from all-atom simulations. Without extending the spatial dimensionality, the $F(F-1)/2$ reorganization energy restrictions cannot be satisfied simultaneously. The MSH equilibrium shifts $\{S_j^{(XY)}\}$ are given in Appendix A.

Generally, setting $\{S_j^{(i,X)}\} \equiv 0$ when $i \ge X$, we can rewrite the nuclear Hamiltonian of the electronic state X in eq 26 as

$$\hat{H}_X = \sum_{i=1}^{F-1}\sum_{j=1}^{N}\left[\frac{\hat{P}_{i,j}^2}{2} + \frac{1}{2}\tilde{\omega}_j^2(\hat{R}_{i,j} - S_j^{(i,X)})^2\right] + \varepsilon_X \tag{29}$$

The electronic couplings $\{\Gamma_{XY}\}$ can be obtained from the fragment charge difference (FCD) method.[79] The energy minima $\{\varepsilon_X\}$ are determined from their difference, or the reaction free energies $\Delta E^{(XY)}$, which can be estimated with the reorganization energy and the energy-gap average from equilibrium MD simulations on the PES of the initial electronic state[53]

$$\varepsilon_Y - \varepsilon_X = \Delta E^{(XY)} = -E_r^{(XY)} - \langle U_{XY} \rangle \tag{30}$$

2.4. Multistate Reaction Coordinate Model. In this section, we propose the multistate reaction coordinate (MRC) model and show that the MSH model can be translated to the equivalent MRC model. We expect the MRC model to have the same DOF as the MSH model, which is defined in $F-1$ extended dimensions for each normal mode in an F-state system. First, starting from the F-state Hamiltonian in eq 25, we propose the CL or GOA type of primary/secondary potential for each nuclear subspace in each electronic state $\hat{\mathbf{r}}_i = (\hat{y}_i, \{\hat{x}_{i,\alpha} | \alpha = 1, ..., N-1\})$, where $i = 1, ..., F-1$, and the nuclear Hamiltonian of the X-th electronic state is given by

$$\hat{H}_X = \sum_{i=1}^{F-1}\hat{H}_{i,X} + \varepsilon_X, \quad (X = 1, ..., F) \tag{31}$$

where the i-th subspace component is ($S^{(i,X)} \equiv 0$ when $i \ge X$)

$$\hat{H}_{i,X} = \frac{\hat{p}_i}{2} + \frac{1}{2}\Omega^2(\hat{y}_i - S^{(i,X)})^2 + \sum_{\alpha=1}^{N-1}\left[\frac{\hat{p}_{i,\alpha}}{2} + \frac{1}{2}\omega_\alpha^2\left(\hat{x}_{i,\alpha} + \frac{c_\alpha}{\omega_\alpha^2}\hat{y}_i\right)^2\right] \tag{32}$$

Consider the first two states in the first subspace of the MSH model, which is reduced to the asymmetric spin-boson model in eq 14 and the potential energy part is

$$\begin{pmatrix} \sum_{j=1}^{N}\frac{1}{2}\tilde{\omega}_j^2\hat{R}_j^2 & \\ & \sum_{j=1}^{N}\frac{1}{2}\tilde{\omega}_j^2(\hat{R}_j - R_j^{eq})^2 \end{pmatrix} \tag{33}$$

We apply the Householder reflection[80] procedure proposed by Wang and Thoss to transform the normal-mode picture into the primary/secondary-mode picture.[27] The reaction coordinate $\hat{y}$ with normalization factor κ is assigned to be the linear term $\sum_{j=1}^{N}\tilde{\omega}_j^2 R_j^{eq}\hat{R}_j$ in eq 14 that differs from two states such that

$$\hat{y} = \frac{1}{\kappa}\sum_{j=1}^{N}\tilde{\omega}_j^2 R_j^{eq}\hat{R}_j \tag{34}$$

https://doi.org/10.1021/acs.jctc.3c00770
J. Chem. Theory Comput. 2023, 19, 7151−7170

$$\kappa = \sqrt{\sum_{j=1}^{N} \tilde{\omega}_j^2 R_j^{\mathrm{eq}}} \tag{35}$$

By definition, the reorganization energy between these two states is the energy difference between the acceptor-state potential energies evaluated at the equilibrium position of the donor surface and the minimum of the acceptor potential energy. For the two-state primary/secondary-mode case below

$$\begin{pmatrix} \frac{1}{2}\Omega^2\hat{y}^2 & 0 \\ 0 & \frac{1}{2}\Omega^2\left(\hat{y} - \frac{\kappa}{\Omega^2}\right)^2 \end{pmatrix} + \sum_{\alpha=1}^{N-1} \frac{1}{2}\omega_\alpha^2\left(\hat{x}_\alpha + \frac{c_\alpha}{\omega_\alpha^2}\hat{y}\right)^2 \tag{36}$$

we expect the reorganization energy to be equal to eq 16, namely

$$E_r = \frac{1}{2}\frac{\kappa^2}{\Omega^2} = \sum_{j=1}^{N} \frac{1}{2}\tilde{\omega}_j^2 (R_j^{\mathrm{eq}})^2 \tag{37}$$

which leads to primary mode frequency

$$\Omega^2 = \frac{\kappa^2}{\sum_{j=1}^{N} \tilde{\omega}_j^2 (R_j^{\mathrm{eq}})^2} \tag{38}$$

Using eqs 36 and 37, we have the equilibrium position distance of the primary mode between the two states

$$\frac{\kappa}{\Omega^2} = \frac{\sqrt{2E_r}}{\Omega} \tag{39}$$

It is noted that the primary mode $\hat{y}$ and its characteristic frequency Ω do not scale with R_j^{eq}, which will be used in the multistate extension. Denoting the expansion coefficients of the primary mode as $u_j = \tilde{\omega}_j^2 R_j^{\mathrm{eq}}$, we express the reaction coordinate vector in the original normal mode basis $\{|R_1\rangle, |R_2\rangle, ..., |R_N\rangle\}$ as

$$|z_1\rangle = \frac{1}{\kappa}\begin{pmatrix} u_1 \\ u_2 \\ \vdots \\ u_N \end{pmatrix} \tag{40}$$

The Householder reflection operator is defined as

$$\mathcal{P} \equiv 1 - 2|\Delta\rangle\langle\Delta| \tag{41}$$

where

$$|\Delta\rangle = \frac{|\delta\rangle}{\sqrt{\langle\delta|\delta\rangle}} \quad \text{and} \quad |\delta\rangle = |z_1\rangle - |R_1\rangle \tag{42}$$

The $\mathcal{P}$ reflects any vector about the plane perpendicular to the difference between the original normal mode $|R_1\rangle$ and the reaction coordinate $|z_1\rangle$, and it satisfies $\mathcal{P}|R_1\rangle = |z_1\rangle$, $\mathcal{P}|z_1\rangle = |R_1\rangle$, $\mathcal{P} = \mathcal{P}^T = \mathcal{P}^{-1}$. Applying this reflector to all the normal mode vectors, we have a new set of orthonormal vectors:

$$|z_j\rangle = \mathcal{P}|R_j\rangle, \quad (j = 1, 2, ..., N) \tag{43}$$

Denoting the coordinates of the normal modes and the new basis as column vectors $\mathbf{R} = (R_1, R_2, ..., R_N)^T$ and $\mathbf{z} = (z_1, z_2, ..., z_N)^T$, respectively, we express the harmonic potential about its equilibrium position as

$$\begin{aligned} V &= \frac{1}{2}\mathbf{R}^T \,\mathrm{diag}(\tilde{\omega}_1^2, ..., \tilde{\omega}_N^2)\mathbf{R} \\ &= \frac{1}{2}\mathbf{z}^T\mathcal{P}\,\mathrm{diag}(\tilde{\omega}_1^2, ..., \tilde{\omega}_N^2)\mathcal{P}\mathbf{z} = \frac{1}{2}\mathbf{z}^T\mathbf{K}\mathbf{z} \end{aligned} \tag{44}$$

Here, the new Hessian $\mathbf{K}$ in the $\{|z_j\rangle\}$ basis is defined as

$$\mathbf{K} \equiv \mathcal{P}\,\mathrm{diag}(\tilde{\omega}_1^2, ..., \tilde{\omega}_N^2)\mathcal{P} = \begin{pmatrix} K_{11} & \langle d| \\ |d\rangle & \mathbf{K}_{\mathrm{sub}} \end{pmatrix} \tag{45}$$

where $\mathbf{K}_{\mathrm{sub}}$ is the last $(N-1) \times (N-1)$ block of Hessian matrix $\mathbf{K}$, $(N-1)$-dim vector $\langle d| = (K_{21}, K_{31}, ..., K_{N1})$, and element

$$K_{11} = \frac{1}{\kappa^2}\sum_{j=1}^{N} u_j^2\tilde{\omega}_j^2 \tag{46}$$

To get orthogonal secondary bath modes, we diagonalize the sub-Hessian matrix $\mathbf{K}_{\mathrm{sub}}$ by orthogonal transformation and obtain the bath frequencies

$$\mathbf{U}^T\mathbf{K}_{\mathrm{sub}}\mathbf{U} = \mathrm{diag}(\omega_1^2, \omega_2^2, ..., \omega_{N-1}^2) = \mathbf{\Lambda} \tag{47}$$

which leads to the block transformation

$$\begin{pmatrix} 1 & \langle 0| \\ |0\rangle & \mathbf{U}^T \end{pmatrix}\begin{pmatrix} K_{11} & \langle d| \\ |d\rangle & \mathbf{K}_{\mathrm{sub}} \end{pmatrix}\begin{pmatrix} 1 & \langle 0| \\ |0\rangle & \mathbf{U} \end{pmatrix} = \begin{pmatrix} K_{11} & \langle c| \\ |c\rangle & \mathbf{\Lambda} \end{pmatrix} = \mathbf{D} \tag{48}$$

Here, the primary/secondary coupling coefficients are

$$|c\rangle = \begin{pmatrix} c_1 \\ c_2 \\ \vdots \\ c_{N-1} \end{pmatrix} = \mathbf{U}^T|d\rangle = \mathbf{U}^T\begin{pmatrix} K_{21} \\ K_{31} \\ \vdots \\ K_{N1} \end{pmatrix} \tag{49}$$

the primary mode $\hat{y} = z_1$, and the secondary modes $(x_1, ..., x_{N-1})$ are transformed as

$$\begin{pmatrix} \hat{x}_1 \\ \hat{x}_2 \\ \vdots \\ \hat{x}_{N-1} \end{pmatrix} = \mathbf{U}^T\begin{pmatrix} z_2 \\ z_3 \\ \vdots \\ z_N \end{pmatrix} \tag{50}$$

and the potential in eq 44 is finally transformed to the primary/secondary-mode form as below

$$\begin{aligned} V &= \frac{1}{2}(\hat{y}, \hat{x}_1, ..., \hat{x}_{N-1})\begin{pmatrix} K_{11} & \langle c| \\ |c\rangle & \mathbf{\Lambda} \end{pmatrix}\begin{pmatrix} \hat{y} \\ \hat{x}_1 \\ \vdots \\ \hat{x}_{N-1} \end{pmatrix} \\ &= \frac{1}{2}\Omega^2\hat{y}^2 + \sum_{\alpha=1}^{N-1} \frac{1}{2}\omega_\alpha^2\left(\hat{x}_\alpha + \frac{c_\alpha}{\omega_\alpha^2}\hat{y}\right)^2 \end{aligned} \tag{51}$$

Next, we consider the F-state case. Since $\hat{y}$, $\mathbf{\Omega}$, and $\mathbf{K}$ do not scale with R_j^{eq}, the primary/secondary couplings $\{c_\alpha\}$ do not change with the reorganization energy, so the reorganization

https://doi.org/10.1021/acs.jctc.3c00770
J. Chem. Theory Comput. 2023, 19, 7151−7170

energy for different pairs of states will be absorbed to the equilibrium positions of the primary mode. In the MSH model, the equilibrium shifts of the normal modes are built to scale with square roots of the reorganization energies, so we can apply the same polyhedron geometry to the primary mode or the reaction coordinate in the MRC model in $F-1$ dimensions. The transformation matrix $\mathbf{U}$ can be chosen to be the same in different subspaces $i = 1, ..., F-1$, since flipping the sign of any eigenvector does not affect the diagonalization or the eigenvalue. Using eq 39, we have the equilibrium shifts for the primary mode as below (see eq 65 for more details).

$$\mathbf{S} = \begin{pmatrix} S^{(12)} & & \\ S^{(13)} & S^{(23)} & \\ S^{(14)} & S^{(24)} & S^{(34)} \\ & \cdots & \end{pmatrix} = \frac{\sqrt{2}}{\Omega}\begin{pmatrix} A_1^{(12)} & & \\ A_1^{(13)} & A_2^{(13)} & \\ A_1^{(14)} & A_2^{(14)} & A_3^{(14)} \\ & \cdots & \end{pmatrix} \tag{52}$$

Now, we have obtained the model parameters including Ω, $\{\omega_\alpha\}$, $\{c_\alpha\}$, $\{S^{(XY)}\}$ that define the MRC model and rewrite eqs 31 and 32 as below

$$\begin{aligned}
\hat{H}_1 &= \sum_{i=1}^{F-1}\frac{\hat{p}_i}{2} + \frac{1}{2}\Omega^2(\hat{y}_1^2 + \hat{y}_2^2 + \cdots + \hat{y}_{F-1}^2) + \hat{H}_{BC} + \varepsilon_1,\\
\hat{H}_2 &= \sum_{i=1}^{F-1}\frac{\hat{p}_i}{2} + \frac{1}{2}\Omega^2[(\hat{y}_1 - S^{(12)})^2 + \hat{y}_2^2 + \cdots + \hat{y}_{F-1}^2]\\
&\quad + \hat{H}_{BC} + \varepsilon_2,\\
\hat{H}_3 &= \sum_{i=1}^{F-1}\frac{\hat{p}_i}{2} + \frac{1}{2}\Omega^2[(\hat{y}_1 - S^{(13)})^2 + (\hat{y}_2 - S^{(23)})^2 + \cdots\\
&\quad + \hat{y}_{F-1}^2] + \hat{H}_{BC} + \varepsilon_3,\\
&\cdots\\
\hat{H}_F &= \sum_{i=1}^{F-1}\frac{\hat{p}_i}{2} + \frac{1}{2}\Omega^2[(\hat{y}_1 - S^{(1F)})^2 + (\hat{y}_2 - S^{(2F)})^2 + \cdots\\
&\quad + (\hat{y}_{F-1} - S^{(F-1,F)})^2] + \hat{H}_{BC} + \varepsilon_F
\end{aligned} \tag{53}$$

where $\hat{H}_{BC}$ for the secondary bath and the primary/secondary coupling is given by

$$\hat{H}_{BC} = \sum_{i=1}^{F-1}\sum_{\alpha=1}^{N-1}\left[\frac{\hat{p}_{i,\alpha}}{2} + \frac{1}{2}\omega_\alpha^2\left(\hat{x}_{i,\alpha} + \frac{c_\alpha}{\omega_\alpha^2}\hat{y}_i\right)^2\right] \tag{54}$$

We could translate between the MSH model and the MRC model through Hessian matrix diagonalization, where the Hessian matrix $\mathbf{D}$ is the same as eq 12 for each subspace $\hat{y}_i$, $\{\hat{x}_{i,\alpha}\}$, $(i = 1, ..., F-1)$. The instantaneous positions $(R_{i,1}, R_{i,2}, ..., R_{i,N})$ of the MSH model can be translated into or from the corresponding MRC configuration $(y_i, x_{i,1}, ..., x_{i,N-1})$ using

$$\begin{pmatrix} y_i - S^{(i,X)} \\ x_{i,1} + \frac{c_1}{\omega_1^2}S^{(i,X)} \\ \vdots \\ x_{i,N-1} + \frac{c_{N-1}}{\omega_{N-1}^2}S^{(i,X)} \end{pmatrix} = \mathbf{T}\begin{pmatrix} R_{i,1} - S_1^{(i,X)} \\ R_{i,2} - S_2^{(i,X)} \\ \vdots \\ R_{i,N} - S_N^{(i,X)} \end{pmatrix} \tag{55}$$

Here, the transformation matrix $\mathbf{T}$ is given in eq 13, which requires the knowledge of primary frequency Ω, secondary bath modes' frequencies $\{\omega_\alpha\}$ and their couplings with the primary mode $\{c_\alpha\}$.

It is important to note that transforming from a primary/secondary coupled MRC model to an uncoupled normal-mode MSH model is straightforward, which can be obtained by diagonalizing the Hessian $\mathbf{D}$ as shown in eq 13. However, there are many ways to transform from normal mode parameters in the MSH model to a primary/secondary coupled MRC model, and the current approach described above using Householder reflection provides an effective way of achieving this goal. Moreover, knowing the explicit form of how the primary modes $\{\hat{y}_i\}$ couple with the secondary bath $\{\hat{x}_{i,\alpha}\}$ and $\hat{H}_{BC}$ does not depend on electronic states is important for verifying that $\{\hat{y}_i\}$ indeed serves as RC. Also, it is equally important to prove the equivalence and transformations between MSH and MRC models analytically and numerically, and we will show the numerical comparison in section 4. In principle, this primary/secondary partitioning procedure is not limited to the first layer of RC, so one could keep applying this procedure to achieve a hierarchy of RC layers. The MRC model Hamiltonian provides a convenient and intuitive way of understanding nonadiabatic dynamics in multistate systems.

3. SIMULATION DETAILS

3.1. Model Preparation. We construct the MRC and the MSH models for photoinduced charge transfer dynamics in two CPC_{60} triad conformations with four electronic states, $\{\pi\pi^*, CT1, CT2, G\}$, where conf. #3 was previously reported in ref 54. and conf. #5 is a new one (see Figure 2). Here, in the donor-bridge-acceptor type of organic photovoltaic CPC_{60} triad, the $\pi\pi^*$ state is the porphyrin-localized excited bright state, CP^*C_{60}, CT1 state is a partially charge-separated state, $CP^+C_{60}^-$, CT2 state is a fully charge-separated state, $C^+PC_{60}^-$, and G is the ground electronic state. Confirmations #3 and #5 were sampled from molecular dynamics (MD) simulations on the ground state and selected since their CT2 state gets populated in the first few picoseconds after the initial photoexcitation. CT dynamics is conformation-specific, so

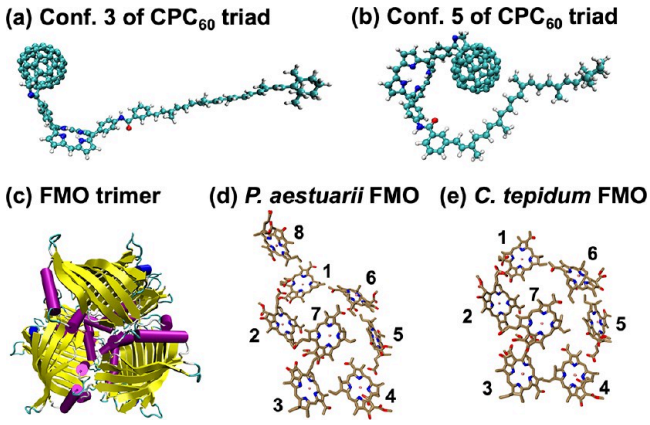

Figure 2. Molecular conformations of carotenoid-porphyrin-C_{60} (CPC_{60}) triad including conformation #3 (a) and conformation #5 (b) as well as the light-harvesting Fenna-Matthews-Olson (FMO) complex trimer of *P. aestuarii* (c), 8 BChl sites in *P. aestuarii* FMO complex, and 7 BChl sites in *C. tepidum* FMO complex.

https://doi.org/10.1021/acs.jctc.3c00770
J. Chem. Theory Comput. 2023, 19, 7151−7170

one might have to resort to a statistical description for an ensemble of conformations at finite temperatures, such as the CT landscape predicted by machine learning.[81] In both MRC and MSH models, the number of physical normal modes N = 200 and the total nuclear DOF is $N_n = (F-1) \times N = 600$. The energy minima, interstate couplings, energy corrections, and reorganization energies are summarized in Table 1. The mode frequencies and the equilibrium shifts along with other MRC model parameters are provided in the Supporting Information.

Table 1. Energy Minima, Interstate Couplings, Energy Corrections, and Reorganization Energies for Confirmations 3 and 5[a]

	conf. 3	conf. 5
$\varepsilon_1(\pi\pi^*)$	0	0
ε_2(CT1)	−0.828	−0.758
ε_3(CT2)	−0.640	−1.128
ε_4(G)	0	0
$W_1(\pi\pi^*)$	0.728	1.551
W_2(CT1)	−2.103	−0.697
W_3(CT2)	−2.131	−0.650
W_4(G)	0	0
Γ_{12}	-1.5×10^{-2}	8.1×10^{-2}
Γ_{13}	7.2×10^{-3}	4.1×10^{-3}
Γ_{23}	-2.9×10^{-2}	-3.2×10^{-3}
Γ_{Y4}	0	0
$E_r^{(12)}$	7.880	6.464
$E_r^{(13)}$	11.39	18.68
$E_r^{(14)}$	0.9202	20.22
$E_r^{(23)}$	3.546	0.3096
$E_r^{(24)}$	21.23	7.920
$E_r^{(34)}$	26.42	18.95
Ω	198.93	228.47

[a]Energy minima ε_X and energy corrections W_X of four electronic states, electronic couplings Γ_{XY} and reorganization energies $E_r^{(XY)}$ (unit kcal/mol) between different pairs of states in the two conformations (#3 and #5) of the triad (unit in eV), as well as the reaction coordinate frequencies Ω (unit in cm^{-1}). Here, electronic states X = 1, 2, 3, and 4 correspond to $\pi\pi^*$, CT1, CT2, and ground (G) states, respectively. The electronic couplings between any excited states (Y < 4) and the ground state are assumed to be zero.

To obtain the MRC model parameters, we performed MD simulations for calculating the energy-gap time correlation functions (eq 17), and thus the spectral densities (eq 18) and the reorganization energies (eq 19). MD simulation of a 70 Å × 70 Å × 70 Å periodic box containing a triad on the $\pi\pi^*$ state and 2700 THF solvents at 300 K was done using the PMEMD program of AMBER20 package.[82] Particle Mesh Ewald summation was used to calculate the electrostatic interactions.[83] The van der Waals and real-space PME cutoff radii were set to 9.0 Å. The time step of the MD simulation was set to δt = 1 fs. The triad conformation was kept rigid with a steep harmonic constraint of force constant 100 kcal mol^{-1} $Å^{-2}$, and SHAKE[84] algorithm was used to constrain all covalent bonds involving hydrogen atoms. The MD simulation follows the steps below. First, the system was minimized for 1000 steps with the steepest descent method, which is followed by 39000 steps of conjugate gradient minimization with an initial step length of 0.01 ps. Second, the system was heated from 0 to 300 K for 20 ps and relaxed for 80 ps at 300 K under the Langevin thermostat with a collision frequency of 2.0 ps^{-1}. Third, the system was equilibrated under isothermal−isobaric (NPT) ensemble at 300 K and 1 bar for 500 ps with Langevin thermostat with a collision frequency of 1.0 ps^{-1} and Berendsen barostat with a pressure relaxation time of 0.5 ps and compressibility of 4.46×10^{-5} bar, and the final averaged box size is 71.524 Å × 71.595 Å × 71.500 Å. Fourth, 200 independent initial conditions including configurations and velocities were sampled from a canonical (NVT) ensemble at 300 K with a Langevin thermostat with a collision frequency of 1.0 ps^{-1} every 20 ps after re-equilibration of 500 ps. Fifth, starting from each initial condition, after relaxation of 50 ps, a microcanonical (NVE) trajectory of 100 ps was generated and configurations were saved every 5 fs, which was used to recalculate the potential energies on other electronic states using

$$V_X(\mathbf{R}) = V_X^{\mathrm{MD}}(\mathbf{R}) + E_X(\mathbf{r}^{\mathrm{triad}}) - V_X(\mathbf{r}^{\mathrm{triad}}) = V_X^{\mathrm{MD}}(\mathbf{R}) + W_X \quad (56)$$

Here, $V_X^{\mathrm{MD}}(\mathbf{R})$ is the MD potential energy of the whole system with the triad on its X excited state calculated by the force field in the general AMBER force field (GAFF)[85] form but atomic charges replaced with those from electronic structure calculation. $E_X(\mathbf{r}^{\mathrm{triad}})$ is the energy of the gas-phase triad on the X excited state obtained from electronic structure calculation, $V_X(\mathbf{r}^{\mathrm{triad}})$ is the gas-phase triad energy on the X excited state obtained from the force field, and W_X is the energy correction for the excitation energy for the triad on the X excited state.[71] Sixth, using the 200 independent NVE trajectories, we calculated the energy gap TCFs $C_{UU}^{(XY)}(t)$ with a time interval of 5 fs and up to 11 ps, from which we obtain the spectral densities (see Figure 3) and reorganization energies

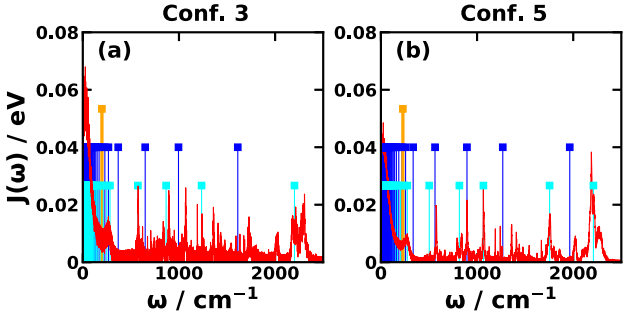

Figure 3. Spectral density (red), reaction coordinate frequency (orange), and secondary bath mode frequencies (blue) of MRC model, and normal-mode frequencies of MSH model (cyan) for CPC_{60} triad conformations #3 and #5 obtained with all-atom simulations at 300 K.

(see Table 1) between pairs of states. The resulting reaction coordinate frequencies Ω for conf. #3 and conf. #5 are given in Table 1 and they range from 200 to 228 cm^{-1} corresponding to typical intermolecular motion in the liquid phase. The equilibrium shift matrix (in a.u.) defined in eq 52 for conf. #3 and conf. #5 are given respectively by

$$\mathbf{S} = \begin{pmatrix} 174.842 & 0 & 0 \\ 203.530 & 52.4113 & 0 \\ -108.812 & -2.45914 & 43.7097 \end{pmatrix} \quad (57)$$

https://doi.org/10.1021/acs.jctc.3c00770
J. Chem. Theory Comput. 2023, 19, 7151−7170

$$\mathbf{S} = \begin{pmatrix} 137.880 & 0 & 0 \\ 52.5044 & 228.440 & 0 \\ -12.2267 & 3.08265 & 27.4126 \end{pmatrix} \quad (58)$$

The electronic couplings between different states $\{\Gamma_{XY}\}$ (see Table 1) were obtained by using the FCD method. The energy minima $\{\varepsilon_X\}$ (see Table 1) were obtained from time-dependent density functional theory (TDDFT) calculations[71,86] and the average energy gap from MD simulation using eq 30. The TDDFT calculation for the triad was performed with the range-separated hybrid (RSH) Baer-Neuhauser-Livshits (BNL) functional (range-separation parameter $\omega = 0.157$) in SV basis using QChem 4.4.[87] Since the ground state is only for initial nuclear sampling and it does not have electronic couplings with the three excited states in the model, the energy minimum parameter ε_G does not affect the dynamics and thus can be chosen arbitrarily.

The MRC models for excitation energy transfer in the photosynthetic light-harvesting FMO complex were constructed for 7 bacteriochlorophyll (BChl) sites in the *C. tepidum* FMO complex and 8 BChl sites in the *P. aestuarii* FMO complex (see Figure 2), corresponding to Protein Data Bank (PDB) identification numbers 3ENI and 3EOJ, respectively. The FMO complexes in *C. tepidum* and *P. aestuarii* have different absorption spectra and thus different excitation energies and EET dynamics.[40,41,44,45,55,72−76] In fact, the *C. tepidum* FMO complex also has the eighth BChl site, but since historically the 7-site model has been widely used for quantum dynamics calculations, we decided to test the 7-site model.[40] The MSH model parameters for 7-site *C. tepidum* and 8-site *P. aestuarii* FMO complexes were reported in ref 55. The model is based on all-atom quantum-mechanics/molecular-mechanics (QM/MM) simulation of the entire FMO trimer in explicit water.[44,45] We refer the reader to ref 55 for more model parameters including the site energies, electronic couplings, and pairwise reorganization energies. It is noted that with the additional ground state the 7-site and 8-site MSH/MRC models correspond to $F = 8$ and $F = 9$, respectively. The physical nuclear modes for both *C. tepidum* and *P. aestuarii* FMO complexes are $N = 100$, and total nuclear DOF $N_n = (F - 1) \times N$. Following the procedure introduced in the previous section, we translated the MSH model to the MRC model and obtained that the reaction coordinate frequencies for the 7-site *C. tepidum* and the 8-site *P. aestuarii* FMO complexes are 1187.2 and 507.68 cm^{-1}, respectively. The MRC model parameters for both FMO complexes are provided in the Supporting Information.

3.2. Nonadiabatic Dynamics Simulations. In most photoinduced chemical dynamics, the initial state of the overall system can be assumed to be given by the overall density operator

$$\hat{\rho}(0) = \hat{\rho}_N(0) \otimes \hat{\sigma}(0) = \sum_{m,n}^{F} \hat{\rho}_N(0)\sigma_{mn}(0)|m\rangle\langle n| \quad (59)$$

where the initial nuclear and electronic reduced density matrices (RDM) are given by $\hat{\rho}_N(0) = \mathrm{Tr}_e[\hat{\rho}(0)]$ and $\hat{\sigma}(0) = \mathrm{Tr}_N[\hat{\rho}(0)] = \sum_{m,n}^{F} \sigma_{mn}(0)|m\rangle\langle n|$, respectively, and $\mathrm{Tr}_e[\cdot]$ and $\mathrm{Tr}_N[\cdot]$ denote partial trace over the electronic and nuclear Hilbert spaces, respectively. The dynamics of the electronic RDM at time t after the photoexcitation is of interest, i.e.,

$$\sigma_{jk}(t) = \sum_{m,n}^{F} \sigma_{mn}(0)\mathrm{Tr}_N\mathrm{Tr}_e[\hat{\rho}_N(0)|m\rangle\langle n|e^{i\hat{H}t/\hbar}|k\rangle\langle j|e^{-i\hat{H}t/\hbar}] \quad (60)$$

where the diagonal elements $\sigma_{jj}(t)$ are electronic populations and the off-diagonal elements $\sigma_{jk}(t)$ $(j \neq k)$ are electronic coherences.

Usually, in photoinduced CT or EET processes, one usually considers the case of starting from a population of a certain electronic state, say, $\hat{\sigma}(0) = |m\rangle\langle m|$ or $\sigma_{mm}(0) = 1$ and all other initial RDM elements vanish. In our simulations, we start from the $|\pi\pi^*\rangle\langle\pi\pi^*|$ population for the triad that mimics the result of vertical excitation from the ground state (or other nonequilibrium state) to the $\pi\pi^*$ state, and the FMO complex in the initial excitation populates the BChl site 1 in both *C. tepidum* and *P. aestuarii* FMO complexes, namely $|1\rangle\langle 1|$.

The initial nuclear conditions including positions and momenta correspond to the Wigner transform of $\hat{\rho}_N(0)$, which can be the ground state or an arbitrary state:

$$\begin{aligned} \rho_W^{(i)}(\mathbf{R}_0, \mathbf{P}_0) &= \int \mathrm{d}\mathbf{Z}\, e^{-i\mathbf{Z}\cdot\mathbf{P}_0/\hbar} \left\langle \mathbf{R}_0 + \frac{\mathbf{Z}}{2} \middle| \hat{\rho}_N(0) \middle| \mathbf{R}_0 - \frac{\mathbf{Z}}{2} \right\rangle \\ &= \prod_j^{N_n} \frac{1}{\pi\hbar} \tanh\left(\frac{\beta\hbar\omega_j}{2}\right) \\ &\quad \times \exp\left[-\frac{2}{\hbar\omega_j} \tanh\left(\frac{\beta\hbar\omega_j}{2}\right) H_i(\mathbf{R}_0, \mathbf{P}_0) \right] \end{aligned} \quad (61)$$

where $\beta = 1/k_B T$ and $T = 300$ K, N_n is the total nuclear DOF, and $H_i(\mathbf{R}_0, \mathbf{P}_0)$ is the classical harmonic nuclear Hamiltonian that dictates the initial nuclear state. To have consistent initial nuclear conditions, we sample in the MSH model and transform to the MRC model as shown in eq 55.

The nonadiabatic dynamics of the MSH and the MRC models for triad and FMO systems were simulated using nonadiabatic semiclassical dynamics methods that were recently employed,[53,54] including Ehrenfest mean-field (MF),[88] resolution of identity linearized semiclassical mapping No. 1 (RI-LSC1),[38,39] symmetrical quasi-classical dynamics with triangle window (SQC),[35] and spin-mapping approach in W scheme (SPM).[89] These approaches could be regarded as mapping dynamics methods where the electronic DOF are represented as the Meyer-Miller-Stock-Thoss mapping variables,[90,91] if we consider MF as the special case when the zero-point energy parameter vanishes. It should be noted that the main point here is to test the equivalence between MSH and MRC models under different methods rather than discussing the performance or accuracy of different dynamical methods. In our nonadiabatic simulations, the nuclear DOF is propagated using the velocity-Verlet algorithm, electronic mapping variables are propagated using the fourth-order Runge−Kutta algorithm, and mapping variables update 20 times per nuclear step. For both MSH and MRC models of the triad system, the nuclear time step was chosen as $\delta t = 0.1$ fs and the electronic population dynamics was obtained by averaging over 10^5 trajectories, except for the RI-LSC1 method, which was over 10^6 trajectories; for both MSH and MRC models of the FMO complex, the nuclear time step was chosen as $\delta t = 1$ fs and the electronic population dynamics was obtained by averaging over 10^6 trajectories. The computational costs for both MSH and MRC models are almost the same; for

https://doi.org/10.1021/acs.jctc.3c00770
J. Chem. Theory Comput. 2023, 19, 7151−7170

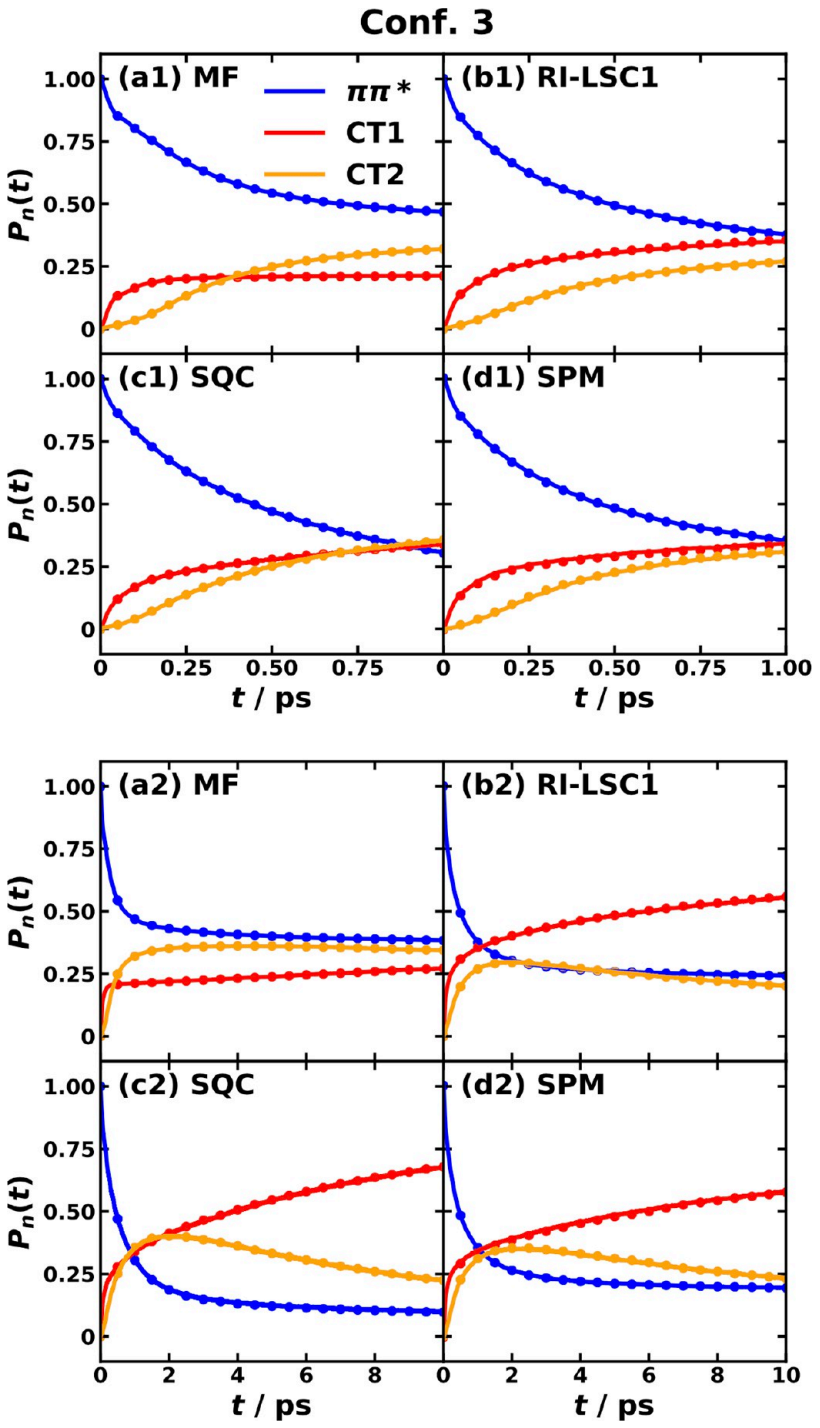

Figure 4. Photoinduced CT population dynamics for MSH model (solid lines) and MRC model (dots) of the CPC_{60} triad conformation #3 obtained with different semiclassical dynamics at 300 K. The initial electronic state is $|\pi\pi^*\rangle\langle\pi\pi^*|$ and the initial nuclear state is in thermal equilibrium with the ground state potential energy surface.

example, for a triad conformation 140 core-hours (e.g., Intel Xeon Gold 6132 Central Processing Unit with 2.6 GHz base frequency) would be required to sample over 10^6 trajectories of 10 ps each.

4. RESULTS AND DISCUSSION

In this section, we first present the photoinduced CT dynamics in the CPC_{60} triad of two different conformations in the solution phase as well as the EET dynamics in photosynthetic light-harvesting FMO complexes in *C. tepidum* and *P. aestuarii* obtained with corresponding MSH and MRC models at 300 K. It is noted that the main focus here is to test the equivalence between MSH and MRC models, which is expected since the mathematical transformation between the two models is exact.

Figures 4 and 5 display the comparison between MSH and MRC models for conf. #3 and conf. #5 of the CPC_{60} triad, respectively. It is evident that the nonadiabatic dynamics produced by using MSH and MRC models are identical within the same dynamical method, which validates the equivalence between the MSH and MRC model Hamiltonians. As we

https://doi.org/10.1021/acs.jctc.3c00770
J. Chem. Theory Comput. 2023, 19, 7151−7170

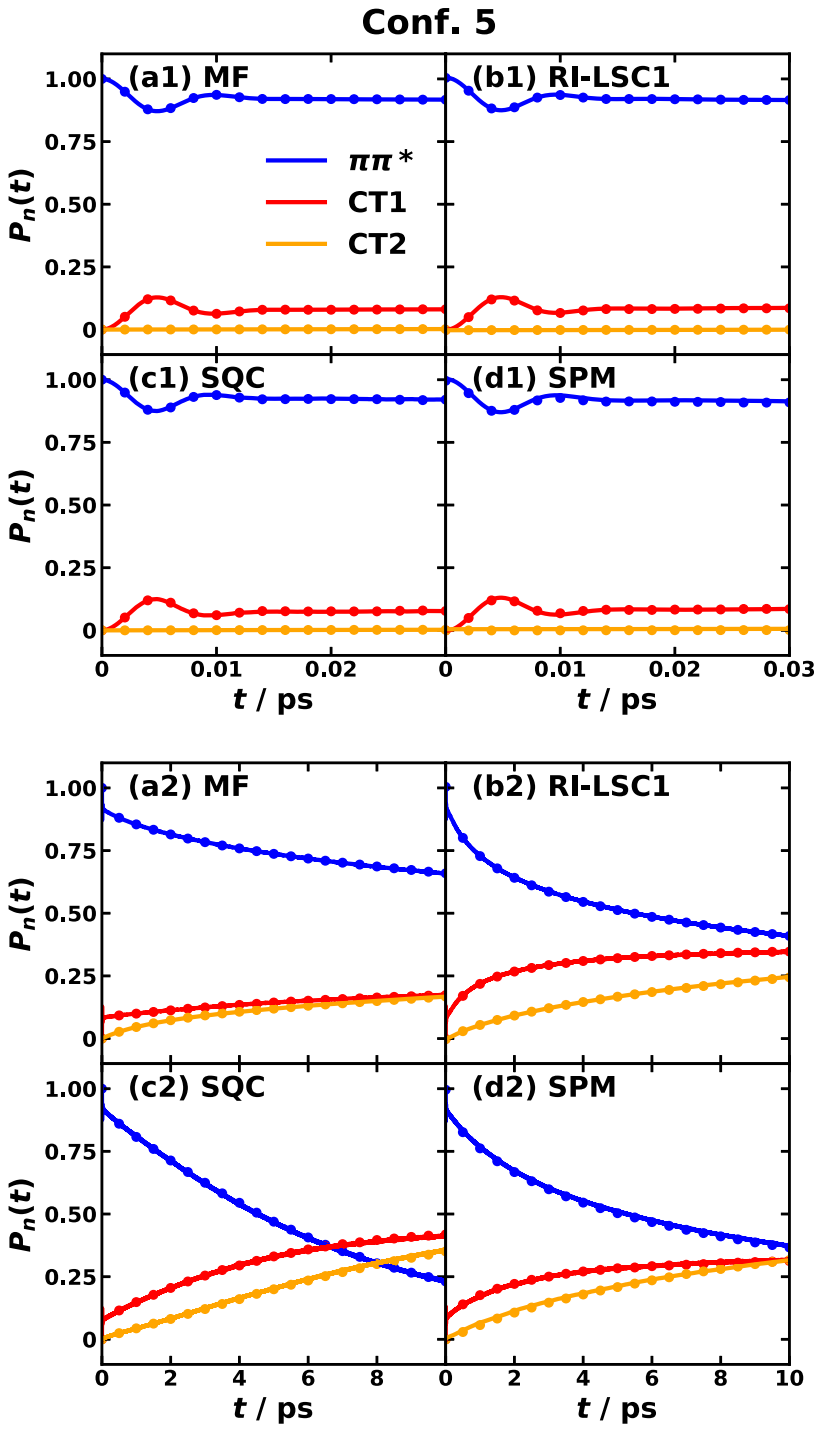

Figure 5. Photoinduced CT population dynamics for the MSH model (solid lines) and MRC model (dots) of the CPC_{60} triad conformation #5 obtained with different semiclassical dynamics at 300 K. The initial electronic state is $|\pi\pi^*\rangle\langle\pi\pi^*|$ and the initial nuclear state is in thermal equilibrium with the ground state potential energy surface.

checked, the numerical results of the electronic populations obtained with MSH and MRC Hamiltonians are the same within 11 significant figures in the first tens of steps and within 7 significant figures at 1 ps. It is believed that this small difference in populations between MSH and MRC models is due to the numerical error in the computer's double precision, rather than the transformation formula.

For triad conf. #3, the short- and long-time population dynamics are plotted as the upper and lower panel groups of Figure 4. What we observe is that after the photoexcitation putting the system on the $\pi\pi^*$ excited state but the nuclear DOF are still in equilibrium with the ground state PES, the electronic state population on $\pi\pi^*$ state starts to decay to the other two CT states. In the first 1 ps, the populations of CT1 and CT2 grow to a similar level of about 0.3 crossing with the initial $\pi\pi^*$, while the response time of CT1 is quicker than that of CT2. Then in the longer time scale of 10 ps, the population of CT1 continues to increase gradually, whereas the population of CT2 starts to decrease slightly in RI-LSC1, SQC, and SPM dynamics but not in MF dynamics, which is believed to be less

https://doi.org/10.1021/acs.jctc.3c00770
J. Chem. Theory Comput. 2023, 19, 7151−7170

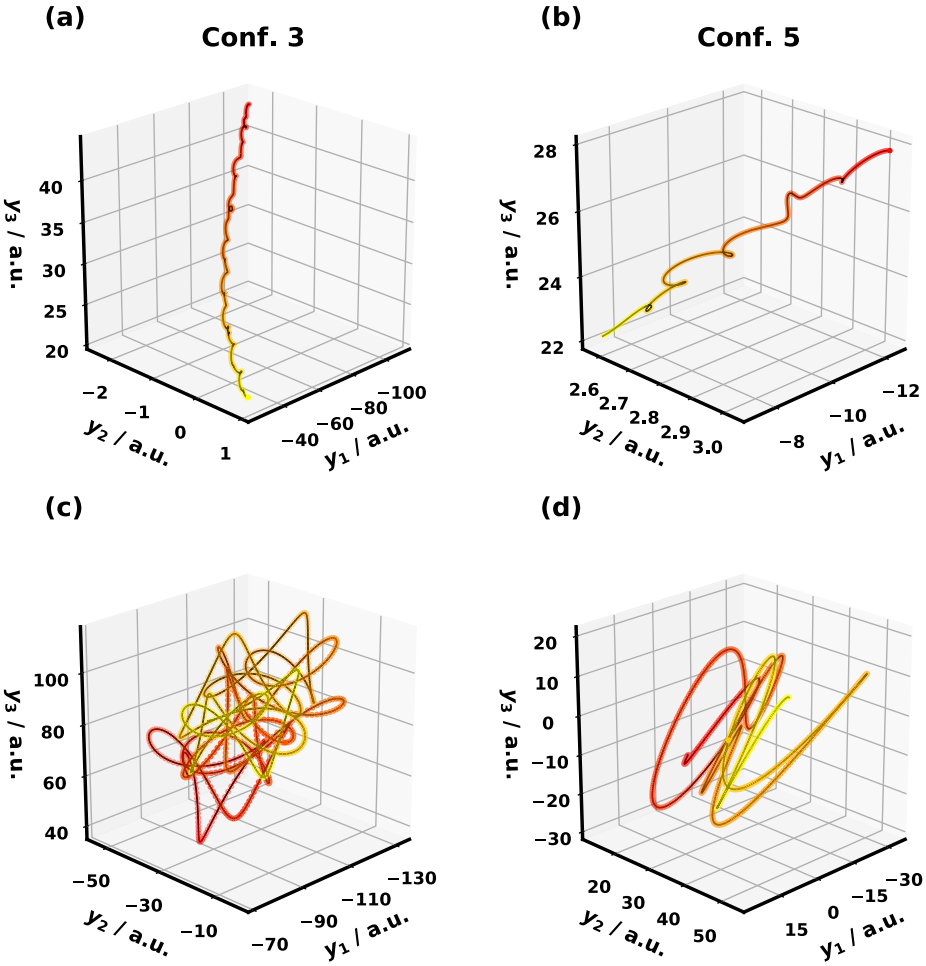

Figure 6. Reaction coordinate trajectory for MRC models of CPC_{60} triad conformation #3 (left) and conformation #5 (right) obtained with the SQC method. Here, top panels (a) and (b) are averaged over 10^5 trajectories; bottom panels (c) and (d) are single sampled trajectories; left panels (a) and (c) show the first 0.3 ps in conformation #3; right panels (b) and (d) show the first 0.1 ps of conformation #5; the color gradient from red to yellow corresponds to the initial and to the final times.

accurate than the other methods. The nonadiabatic dynamics predicted by the MSH model has been demonstrated to agree with that obtained with the explicitly all-atom multistate Hamiltonian in ref 54. The agreement among MSH, MRC, and all-atom Hamiltonians in combination with the same dynamical method suggests the effectiveness of the simplified MSH and MRC models in studying the nonadiabatic dynamics in complex condensed-phase systems.

For triad conf. #5, two separated time scales are observed as shown in Figure 5. Here, an ultrafast population oscillation between the initial $\pi\pi^*$ state and CT1 state in the first 20 fs after photoexcitation is shown in the upper panels of Figure 5, followed by a slow population transfer from $\pi\pi^*$ to CT1 and CT2 in the 10 ps scale shown in the lower panels of Figure 5. For ultrafast dynamics, all four methods give rise to the same result, while for longer-time dynamics, MF predicts a slower transfer rate compared with the other three methods. Besides the electronic RDM dynamics including populations and coherences, we also confirm that the nuclear motions are identical by using MSH and MRC models under the same dynamical method, which suggests that the MSH and MRC models are fully equivalent.

A benefit of MRC models is that the trajectory of the RC is readily available. Figure 6 shows the averaged and single sampled RC trajectories for MRC models of triad conf. #3 and conf. #5 in the first 0.3 and 0.1 ps after the photoexcitation, respectively. The RC trajectories offer an intuitive picture for understanding the photoinduced CT dynamics. For example, the highly averaged RC trajectory exhibits a smooth pathway with a clear trend determined by the inherent driving force, whereas a single trajectory displays a wildly oscillatory feature that masks the trend. Fortunately for all four-state MRC models, we could render the reaction coordinate in a 3-dimensional plot; for any system with more than four states, it would be difficult to plot all RC components together, so one would have to consider the components separately.

We now turn our attention to EET dynamics in photosynthetic FMO complexes in *C. tepidum* and *P. aestuarii* as shown in Figures 7 and 8, respectively. First of all, EET dynamics using the MRC model coincide with that using the MSH model[55] in all cases considered here, including in both *C. tepidum* and *P. aestuarii* FMO complexes using different nonadiabatic dynamics methods. Second, we do observe different EET pathways in *C. tepidum* and *P. aestuarii* FMO complexes even if the initial excitation is localized on BChl site 1, where the populations of BChl site 1 and BChl site 2 do not cross in *C. tepidum* FMO but they do so in *P. aestuarii* FMO. Third, the eighth BChl site is involved in the EET pathway, as shown in the *P. aestuarii* dynamics where the BChl site 8 gets populated in the first 0.2 ps after initial photoexcitation,

https://doi.org/10.1021/acs.jctc.3c00770
J. Chem. Theory Comput. 2023, 19, 7151−7170

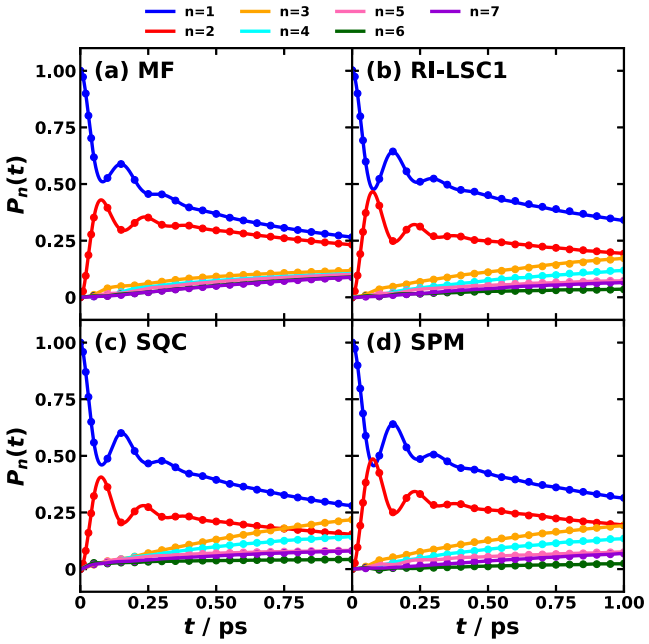

Figure 7. Photoinduced EET population dynamics for MSH model (solid lines) and MRC model (dots) of the 7-site *C. tepidum* FMO complex obtained with different semiclassical dynamics at 300 K. The initial electronic state is $|1\rangle\langle 1|$ and the initial nuclear state is in thermal equilibrium with the ground state potential energy surface.

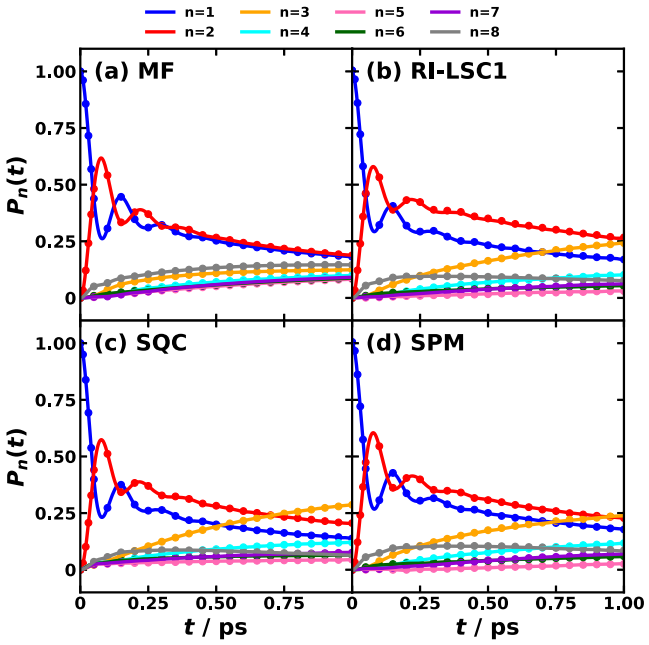

Figure 8. Photoinduced EET population dynamics for MSH model (solid lines) and MRC model (dots) of the 8-site *P. aestuarii* FMO complex obtained with different semiclassical dynamics at 300 K. The initial electronic state is $|1\rangle\langle 1|$, and the initial nuclear state is in thermal equilibrium with the ground state potential energy surface.

especially considering that the spatial location of the BChl site 8 is further away from the final populated BChl site 3. Fourth, both MSH and MRC models incorporate the treatment of static disorder in state-pairwise reorganization energies, realistic spectral density, and state-dependent system-bath couplings. Our previous calculations exhibit that the MSH model with the heterogeneous protein environment description gives rise to a bit slower EET dynamics than the conventional Frenkel exciton model.[55]

We briefly discuss the differences between the MSH/MRC model and the isolated bath model, such as the Frenkel exciton model. The conventional Frenkel exciton model has an overall Hamiltonian given by eq 25 (the same as MSH/MRC model), but the nuclear Hamiltonian of the X-th electronic state is given by

$$\hat{H}_X = \sum_{a=1}^{F}\sum_{j=1}^{N}\frac{\hat{P}_{a,j}^2}{2} + \sum_{j=1}^{N}\frac{1}{2}\tilde{\omega}_j^2\left(\hat{R}_{X,j} - \frac{\tilde{c}_{X,j}}{\tilde{\omega}_j^2}\right)^2 + \sum_{a\neq X}^{F}\sum_{j=1}^{N}\frac{1}{2}\tilde{\omega}_j^2\hat{R}_{a,j}^2 + \varepsilon_X, \quad (X = 1, ..., F) \tag{62}$$

and the ground-state bath Hamiltonian used for determining the initial nuclear condition is given by

$$\hat{H}_B = \sum_{a=1}^{F}\sum_{j=1}^{N}\left(\frac{\hat{P}_{a,j}^2}{2} + \frac{1}{2}\tilde{\omega}_j^2\hat{R}_{a,j}^2\right) \tag{63}$$

Here, the system−bath coupling coefficients $\{\tilde{c}_{a,j}\}$ could in principle depend on the site a, but they are determined only by the spectral density and reorganization energy between the excited state on the a-th site and its ground state, i.e., black double arrows for $E_r^{(Xg)}$ in Figure 1(a). The resulting Frenkel exciton model thus has F independent baths that are coupled to each chromophore site, resulting in a total nuclear DOF of $F \times N$. Thus, it is impossible to incorporate the relations between two excited states in the isolated bath models, such as the Frenkel exciton model. The MSH/MRC models, on the other hand, incorporate all the possible $F(F-1)/2$ state-pairwise reorganization energies, i.e., orange arrows for $E_r^{(XY)}$ and black arrows for $E_r^{(Xg)}$ forming polyhedron in $F-1$ dimensions in Figure 1(b).

The RC trajectories for 8-site *P. aestuarii* and 7-site *C. tepidum* FMO complexes are shown in Figure 9. This is the first time we have seen the time evolution of the nuclear reaction coordinate in the EET dynamics of the FMO complex. The similarities between the 8-site *P. aestuarii* and 7-site *C. tepidum* FMO complexes are seen, but the differences are more interesting to note. For instance, the RC component y_1 that connects the PES minima of $|1\rangle$ and $|2\rangle$ displays a larger oscillation in the 7-site *C. tepidum* FMO, which is consistent with the larger oscillation in the $|1\rangle$ and $|2\rangle$ population dynamics in Figure 7 than the 8-site *P. aestuarii* case in Figure 8. Moreover, there are typically two time scales reflected by the RC dynamics. The first ultrafast time scale is about 500 fs, when all RC components respond to the photoexcitation quickly. The second time scale is about a couple of picoseconds, during which the RC components y_2, y_3, y_4, y_6 in both FMO complexes and the additional y_7 in the *P. aestuarii* FMO complex continue to drift, contributing to the longer EET dynamics that last several picoseconds. We note that the amplitudes of the RC components in the 7-site *C. tepidum* FMO complex are about half of those in the 8-site *P. aestuarii* FMO complex, which can be traced back to the reaction coordinate frequencies of 1187.2 and 507.68 cm^{-1}, respectively. The different RC dynamics in these components indicate a signature of heterogeneity in different BChl sites, along with their protein scaffold environments.

https://doi.org/10.1021/acs.jctc.3c00770
J. Chem. Theory Comput. 2023, 19, 7151−7170

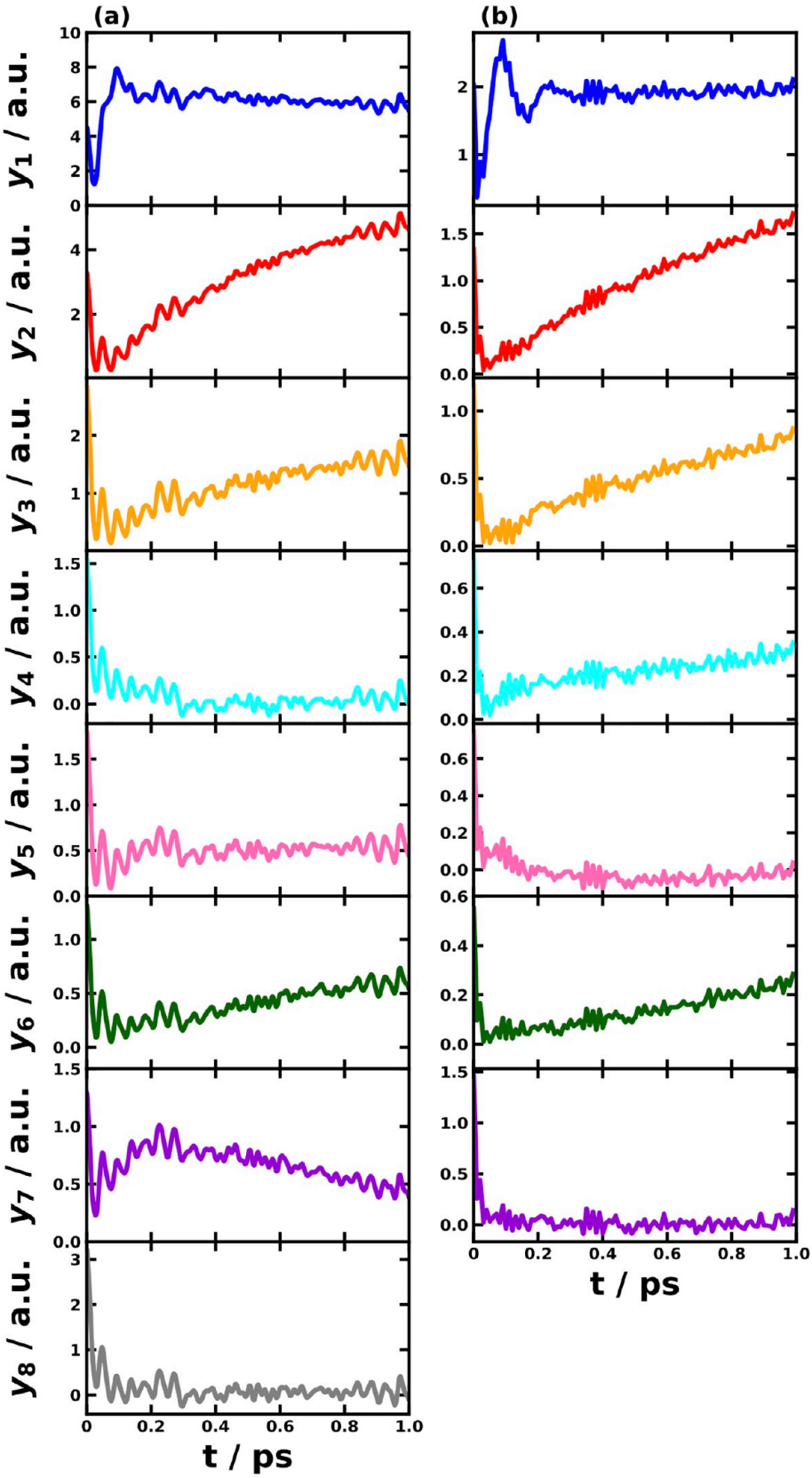

Figure 9. Reaction coordinate trajectories for MRC models of the 8-site *P. aestuarii* FMO complex (a) and 7-site *C. tepidum* FMO complex (b) obtained with averaging 10^6 SQC trajectories.

In fact, heterogeneous environment is crucial in shaping the nonadiabatic dynamics and it is more significant in the photoinduced CT process than in the EET process,[53] which is due to the fact that the CT state interacts with the surrounding environment quite differently from the LE state, thus a large reorganization energy would be expected. Accordingly, we

https://doi.org/10.1021/acs.jctc.3c00770
J. Chem. Theory Comput. 2023, 19, 7151−7170

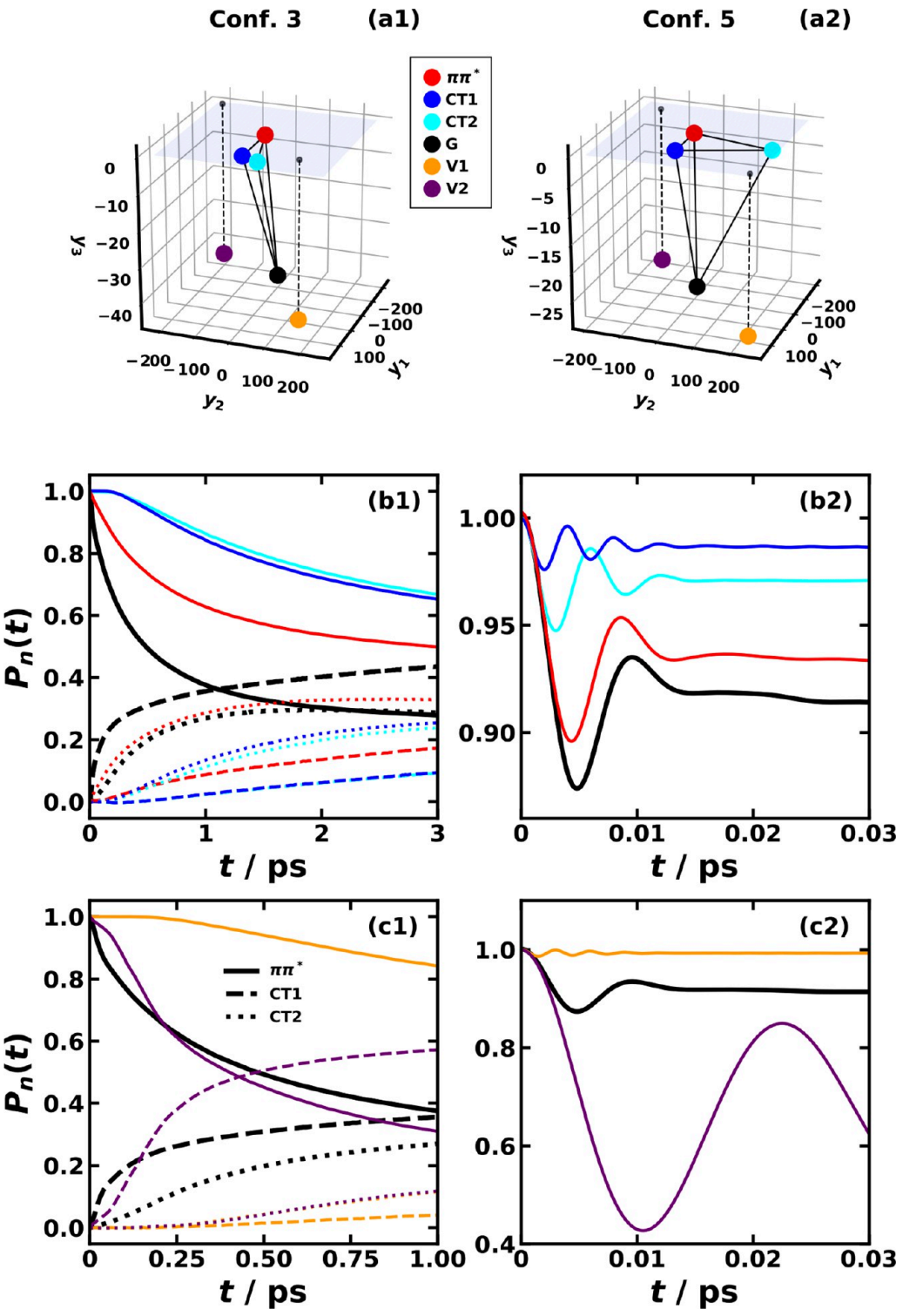

Figure 10. Comparison of nonequilibrium nuclear initial shifts (in a.u.) using MRC models of CPC_{60} triad conformations #3 (left) and #5 (right) indicated as circles in 3-dimensional RC space (a1) and (a2), respectively. The nonadiabatic dynamics are obtained with SQC method at 300 K. The initial electronic state is $|\pi\pi^*\rangle\langle\pi\pi^*|$ in all cases. Panels (b1) and (b2) are cases with the initial nuclear state starting from $\pi\pi^*$ (red), CT1 (blue), and CT2 (cyan) states, and panels (c1) and (c2) are cases with the initial nuclear state starting from arbitrarily chosen V1 (orange) and V2 (purple) states compared with the original case starting from the ground (G, black) state.

believe that it is important to account for the reorganization energies between all pairs of states in studying CT dynamics in a heterogeneous environment. Moreover, even in the case when all chromophores are identical—neglecting molecular orientations and shapes—and they are buried in an identical solvent environment, we would still expect heterogeneous reorganization energies. This is because the intermolecular distances cannot be the same for more than four molecules in our usual three-dimensional space, i.e., four molecules locate at vertices of a regular tetrahedron, and adding one more

https://doi.org/10.1021/acs.jctc.3c00770
J. Chem. Theory Comput. 2023, 19, 7151−7170

molecule would introduce a new pair distance, which will break the equal-distance symmetry. Thus, the treatment for heterogeneous environments is necessary for constructing consistent effective models for multistate systems, such as the approach introduced in parametrizing the MSH or MRC models.

Finally, we would like to show another advantage of the MRC model, i.e., the straightforwardness in starting from an arbitrary nuclear initial state determined by the RC components.[78,92] Taking Figure 10 for the triad system as an example, we visualize the tetrahedron formed by the PES minima of the 4 electronic states in the RC space in 3-dimensions including $\pi\pi^*$, CT1, CT2, and G states, as well as two arbitrary states called V1 and V2 (along with their projections to the upper plain). Note that the initial electronic state is $|\pi\pi^*\rangle\langle\pi\pi^*|$ in all cases, and we only change the initial nuclear state. It is clear that the PES minima distances in conf. #3 and conf. #5 are different; especially, CT1 and CT2 are closer in conf. #3 than in conf. #5 leading to a significant CT2 population in the first couple of picoseconds in conf. #3 (see black dots in Figure 10(b1)). If the initial nuclear state starts from other excited states such as $\pi\pi^*$, CT1, and CT2, the population transfer is actually slower than starting from the ground state as seen in Figure 10(b1,b2) for both conformations. To see the trend of transfer rate enhancement or suppression, we consider the cases starting from two extreme states, i.e., V1 and V2, as shown in Figure 10(c1,c2), and discover that more negative y_1, y_2 values such as the purple V2 lead to faster population transfer, and more positive y_1, y_2 values such as the orange V1 lead to slower population transfer, which is also consistent with the above cases starting from the excited states. The results may shed light on the rational design of more efficient light-harvesting systems by tuning the nuclear distribution.

5. CONCLUDING REMARKS

In this work, we proposed a systematic way to construct MRC model Hamiltonian from all-atom simulations for understanding charge and energy transfer dynamics in complex condensed phases. We do so by first proving the equivalence between the MRC model and the MSH model,[53] which has been shown to consistently account for the heterogeneous correlations between all pairs of states by extending the spatial dimensions to $F-1$ for each normal mode in an F-state system and MSH agrees with all-atom nonadiabatic semiclassical dynamics.[54] The reaction coordinate in an F-state MRC model also has $F-1$ dimensions. The distances between the PES minima of all pairs of states are selected such that the reorganization energies are carried by the reaction coordinate in the extended space, and in the meanwhile, the reaction coordinate bilinearly couples to the secondary bath. In our numerical simulations for the photoinduced CT dynamics in the CPC_{60} triad in the solution phase as well as the EET dynamics in a photosynthetic FMO complex using several nonadiabatic dynamical methods, we confirm that the MRC and the MSH models give rise to the same nonadiabatic dynamics using the same semiclassical dynamical methods, thus demonstrating their equivalence. Besides, MRC model offers an intuitive physical picture for the nuclear-electronic feedback in nonadiabatic processes, such as the inherent average trajectory and the characteristic frequency of the reaction coordinate as well as a straightforward way to incorporate nonequilibrium nuclear initial conditions. Because of these features including mapping from all-atom information, consistently incorporating multistate interstate correlations or reorganization energies, intuitive physical picture using the reaction coordinate in extended dimensions, and nonequilibrium initial state, the MRC model Hamiltonian is believed to provide an effective and robust platform for quantum dissipative dynamics in complex condensed-phase systems. Both MSH and MRC models are based on the harmonic assumption that is expected to be valid for condensed-phase systems, where Gaussian statistics is supported by the central limit theorem and the agreement between MSH model and all-atom nonadiabatic dynamics of the triad.[54] In contrast, the MSH or MRC models are not expected to be accurate in certain single-molecule systems, where anharmonic modes such as isomerization dihedrals might be important. Many quantum dynamical formalisms such as the generalized quantum master equation (GQME)[93−95] are based on the system−bath type of Hamiltonian, and the MRC model can be written in such a way, so MRC model could be naturally adopted for answering the questions regarding realistic systems using such approaches. MRC model could also describe linear vibronic couplings, which will be important for nonadiabatic transitions in conical intersections.[63−65,92,96] Work on using MRC models to investigate the effects of realistic spectral density, state-dependent system−bath couplings, reaction pathways, and heterogeneous environments due to static and dynamical disorder is underway and will be reported in future publications.[3,9,97,98]

A. EQUILIBRIUM SHIFTS IN MSH AND MRC MODELS

As shown in ref 53, the equilibrium shifts in MSH model are proportional to the coordinates of polyhedron vertices

$$\begin{pmatrix} S_j^{(12)} & & & \\ S_j^{(13)} & S_j^{(23)} & & \\ S_j^{(14)} & S_j^{(24)} & S_j^{(34)} & \\ & \cdots & & \end{pmatrix} = a_j \begin{pmatrix} A_1^{(12)} & & & \\ A_1^{(13)} & A_2^{(13)} & & \\ A_1^{(14)} & A_2^{(14)} & A_3^{(14)} & \\ & \cdots & & \end{pmatrix} \tag{64}$$

and as described in the main text, the equilibrium shifts of the reaction coordinate in MRC model are given by

$$\mathbf{S} = \begin{pmatrix} S^{(12)} & & & \\ S^{(13)} & S^{(23)} & & \\ S^{(14)} & S^{(24)} & S^{(34)} & \\ & \cdots & & \end{pmatrix} = \frac{\sqrt{2}}{\Omega} \begin{pmatrix} A_1^{(12)} & & & \\ A_1^{(13)} & A_2^{(13)} & & \\ A_1^{(14)} & A_2^{(14)} & A_3^{(14)} & \\ & \cdots & & \end{pmatrix} \tag{65}$$

Here, the F polyhedron vertices are chosen such that the distances between the PES minima of $F(F-1)/2$ pairs of states are proportional to the corresponding square root of the reorganization energies, $\sqrt{E_r^{(XY)}}$. The positions of the F polyhedron vertices are given by

$$O = (0,0, \ldots, 0) \tag{66}$$

$$A^{(12)} = \sqrt{E_r^{(12)}}\,(1,0, \ldots, 0) \tag{67}$$

$$A^{(13)} = \sqrt{E_r^{(13)}}\,(\cos\theta_{23}, \sin\theta_{23}, 0, \ldots, 0) \tag{68}$$

https://doi.org/10.1021/acs.jctc.3c00770
J. Chem. Theory Comput. 2023, 19, 7151−7170

$$A^{(14)} = \sqrt{E_r^{(14)}}\,(\cos\theta_{24},\ \sin\theta_{24}\cos\theta'_{34},\ \sin\theta_{24}\sin\theta'_{34},\ 0,\ \ldots,\ 0) \tag{69}$$

$$A^{(15)} = \sqrt{E_r^{(15)}}\,(\cos\theta_{25},\ \sin\theta_{25}\cos\theta'_{35},\ \sin\theta_{25}\sin\theta'_{35}\ \cos\theta'_{45},\ \sin\theta_{25}\sin\theta'_{35}\sin\theta'_{45},\ 0,\ \ldots,\ 0) \tag{70}$$

...

$$A^{(1F)} = \sqrt{E_r^{(1F)}}\,(\cos\theta_{2F},\ \sin\theta_{2F}\cos\theta'_{3F},\ \sin\theta_{2F}\sin\theta'_{3F}\ \cos\theta'_{4F},\ \sin\theta_{2F}\sin\theta'_{3F}\sin\theta'_{4F}\cos\theta'_{5F},\ \sin\theta_{2F}\ \sin\theta'_{3F}\sin\theta'_{4F}\sin\theta'_{5F}\cos\theta'_{6F},\ \ldots,\ \sin\theta_{2F}\sin\theta'_{3F}\ \sin\theta'_{4F}\sin\theta'_{5F}\cdots\sin\theta'_{F-2,F}\cos\theta'_{F-1,F},\ \sin\theta_{2F}\ \sin\theta'_{3F}\sin\theta'_{4F}\sin\theta'_{5F}\cdots\sin\theta'_{F-2,F}\sin\theta'_{F-1,F}), \tag{71}$$

where

$$\cos\theta_{jk} = \frac{E_r^{(1j)} + E_r^{(1k)} - E_r^{(jk)}}{2\sqrt{E_r^{(1j)}E_r^{(1k)}}} \tag{72}$$

$$\cos\theta'_{3k} = \frac{\cos\theta_{3k} - \cos\theta_{23}\cos\theta_{2k}}{\sin\theta_{23}\sin\theta_{2k}},\ (k \geq 4) \tag{73}$$

and more generally for $(4 \leq j < k)$:

$$\begin{aligned}\cos\theta'_{jk} = [&\cos\theta_{jk} - \cos\theta_{2j}\cos\theta_{2k} - \sin\theta_{2j}\sin\theta_{2k}\cos\theta'_{3j}\cos\theta'_{3k}\\ &- \sin\theta_{2j}\sin\theta_{2k}\sin\theta'_{3j}\sin\theta'_{3k}\cos\theta'_{4j}\cos\theta'_{4k}\\ &- \sin\theta_{2j}\sin\theta_{2k}\sin\theta'_{3j}\sin\theta'_{3k}\sin\theta'_{4j}\sin\theta'_{4k}\cos\theta'_{57}\cos\theta'_{5k}\\ &-\ldots\\ &- \sin\theta_{2j}\sin\theta_{2k}\sin\theta'_{3j}\sin\theta'_{3k}\sin\theta'_{4j}\sin\theta'_{4k}\\ &\cdots\sin\theta'_{(j-2)j}\sin\theta'_{(j-2)k}\cos\theta'_{(j-1)j}\cos\theta'_{(j-1)k}]\\ &\times[\sin\theta_{2j}\sin\theta_{2k}\sin\theta'_{3j}\sin\theta'_{3k}\sin\theta'_{4j}\sin\theta'_{4k}\cdots\sin\theta'_{(j-2)j}\sin\theta'_{(j-2)k}\\ &\sin\theta'_{(j-1)j}\sin\theta'_{(j-1)k}]^{-1}\end{aligned} \tag{74}$$

■ ASSOCIATED CONTENT

Supporting Information

See the Supporting Information for the . The Supporting Information is available free of charge at https://pubs.acs.org/doi/10.1021/acs.jctc.3c00770.

MRC parameters (ZIP)

MRC model parameters for CPC_{60} triad conformations #3 and #5, and *C. tepidum* and *P. aestuarii* FMO complexes (PDF)

■ AUTHOR INFORMATION

Corresponding Author

Xiang Sun − *Division of Arts and Sciences, NYU Shanghai, Shanghai 200124, China; NYU-ECNU Center for Computational Chemistry at NYU Shanghai, Shanghai 200062, China; Shanghai Frontiers Science Center of Artificial Intelligence and Deep Learning, NYU Shanghai, Shanghai 200124, China; Department of Chemistry, New York University, New York, New York 10003, United States;* orcid.org/0000-0002-2846-8532; Email: xiang.sun@nyu.edu

Authors

Zengkui Liu − *Division of Arts and Sciences, NYU Shanghai, Shanghai 200124, China; NYU-ECNU Center for Computational Chemistry at NYU Shanghai, Shanghai 200062, China; Department of Chemistry, New York University, New York, New York 10003, United States;* orcid.org/0000-0001-6506-9787

Haorui Hu − *Division of Arts and Sciences, NYU Shanghai, Shanghai 200124, China;* orcid.org/0009-0003-9652-6735

Complete contact information is available at: https://pubs.acs.org/10.1021/acs.jctc.3c00770

Notes

The authors declare no competing financial interest.

■ ACKNOWLEDGMENTS

X.S. acknowledges support from the National Natural Science Foundation of China (No. 22273059) and the NYU Shanghai Boost Fund. Computing resources were provided by NYU Shanghai HPC.

■ REFERENCES

(1) Roy, P. P.; Kundu, S.; Valdiviezo, J.; Bullard, G.; Fletcher, J. T.; Liu, R.; Yang, S.-J.; Zhang, P.; Beratan, D. N.; Therien, M. J.; Makri, N.; Fleming, G. R. Synthetic Control of Exciton Dynamics in Bioinspired Cofacial Porphyrin Dimers. *J. Am. Chem. Soc.* **2022**, *144*, 6298−6310.

(2) Wang, D.; Fiebig, O. C.; Harris, D.; Toporik, H.; Ji, Y.; Chuang, C.; Nairat, M.; Tong, A. L.; Ogren, J. I.; Hart, S. M.; Cao, J.; Sturgis, J. N.; Mazor, Y.; Schlau-Cohen, G. S. Elucidating Interprotein Energy Transfer Dynamics within the Antenna Network from Purple Bacteria. *Proc. Natl. Acad. Sci. U.S.A.* **2023**, *120*, No. e2220477120.

(3) Palacino-González, E.; Jansen, T. L. C. Modeling the Effect of Disorder in the Two-Dimensional Electronic Spectroscopy of Poly-3-hexyltiophene in an Organic Photovoltaic Blend: A Combined Quantum/Classical Approach. *J. Phys. Chem. C* **2023**, *127*, 6793−6801.

(4) Wang, J.; Cui, Y.; Chen, Z.; Zhang, J.; Xiao, Y.; Zhang, T.; Wang, W.; Xu, Y.; Yang, N.; Yao, H.; Hao, X.-T.; Wei, Z.; Hou, J. A Wide Bandgap Acceptor with Large Dielectric Constant and High Electrostatic Potential Values for Efficient Organic Photovoltaic Cells. *J. Am. Chem. Soc.* **2023**, *145*, 13686−13695.

(5) Han, G.; Zhang, Y.; Zheng, W.; Yi, Y. Electron Transport in Organic Photovoltaic Acceptor Materials: Improving the Carrier Mobilities by Intramolecular and Intermolecular Modulations. *J. Phys. Chem. Lett.* **2023**, *14*, 4497−4503.

(6) Wang, T.; Chen, Z.-H.; Qiao, J.-W.; Qin, W.; Liu, J.-Q.; Wang, X.-Z.; Pu, Y.-J.; Yin, H.; Hao, X.-T. Correlating Charge Transfer Dynamics with Interfacial Trap States in High-Efficiency Organic Solar Cells. *ACS Appl. Mater. Interfaces* **2023**, *15*, 12109−12118.

(7) Li, Q.; Wang, R.; Zhang, C. The Dynamics of Delocalized Excitations in Organic Solar Cells with Nonfullerene Acceptors. *J. Phys. Chem. Lett.* **2023**, *14*, 3031−3038.

(8) Zhang, G.; Lin, F. R.; Qi, F.; Heumüller, T.; Distler, A.; Egelhaaf, H.-J.; Li, N.; Chow, P. C. Y.; Brabec, C. J.; Jen, A. K.-Y.; Yip, H.-L. Renewed Prospects for Organic Photovoltaics. *Chem. Rev.* **2022**, *122*, 14180−14274.

(9) Vauthey, E. Elucidating the Mechanism of Bimolecular Photoinduced Electron Transfer Reactions. *J. Phys. Chem. B* **2022**, *126*, 778−788.

(10) Giannini, S.; Blumberger, J. Charge Transport in Organic Semiconductors: The Perspective from Nonadiabatic Molecular Dynamics. *Acc. Chem. Res.* **2022**, *55*, 819−830.

(11) Romero, E.; Novoderezhkin, V. I.; van Grondelle, R. Quantum Design of Photosynthesis for Bio-Inspired Solar-Energy Conversion. *Nature* **2017**, *543*, 355−365.
(12) Proppe, A. H.; Li, Y. C.; Aspuru-Guzik, A.; Berlinguette, C. P.; Chang, C. J.; Cogdell, R.; Doyle, A. G.; Flick, J.; Gabor, N. M.; van Grondelle, R.; Hammes-Schiffer, S.; Jaffer, S. A.; Kelley, S. O.; Leclerc, M.; Leo, K.; Mallouk, T. E.; Narang, P.; Schlau-Cohen, G. S.; Scholes, G. D.; Vojvodic, A.; Yam, V. W.-W.; Yang, J. Y.; Sargent, E. H. Bioinspiration in Light Harvesting and Catalysis. *Nat. Rev. Mater.* **2020**, *5*, 828−846.
(13) Ma, Z.; Lin, Z.; Lawrence, C. M.; Rubtsov, I. V.; Antoniou, P.; Skourtis, S. S.; Zhang, P.; Beratan, D. N. How Can Infra-Red Excitation Both Accelerate and Slow Charge Transfer in the Same Molecule? *Chem. Sci.* **2018**, *9*, 6395−6405.
(14) Kurpiers, J.; Ferron, T.; Roland, S.; Jakoby, M.; Thiede, T.; Jaiser, F.; Albrecht, S.; Janietz, S.; Collins, B. A.; Howard, I. A.; Neher, D. Probing the Pathways of Free Charge Generation in Organic Bulk Heterojunction Solar Cells. *Nat. Commun.* **2018**, *9*, 2038.
(15) Wan, X.; Li, C.; Zhang, M.; Chen, Y. Acceptor-Donor-Acceptor Type Molecules for High Performance Organic Photovoltaics − Chemistry and Mechanism. *Chem. Soc. Rev.* **2020**, *49*, 2828−2842.
(16) Chen, Z.; Zhu, H. Photoinduced Charge Transfer and Recombination Dynamics in Star Nonfullerene Organic Solar Cells. *J. Phys. Chem. Lett.* **2022**, *13*, 1123−1130.
(17) Crespo-Otero, R.; Barbatti, M. Recent Advances and Perspectives on Nonadiabatic Mixed Quantum−Classical Dynamics. *Chem. Rev.* **2018**, *118*, 7026−7068.
(18) Prezhdo, O. V. Modeling Non-adiabatic Dynamics in Nanoscale and Condensed Matter Systems. *Acc. Chem. Res.* **2021**, *54*, 4239−4249.
(19) Nelson, T. R.; White, A. J.; Bjorgaard, J. A.; Sifain, A. E.; Zhang, Y.; Nebgen, B.; Fernandez-Alberti, S.; Mozyrsky, D.; Roitberg, A. E.; Tretiak, S. Non-Adiabatic Excited-State Molecular Dynamics: Theory and Applications for Modeling Photophysics in Extended Molecular Materials. *Chem. Rev.* **2020**, *120*, 2215−2287.
(20) Zhang, T.-S.; Fang, Y.-G.; Song, X.-F.; Fang, W.-H.; Cui, G. Hydrogen-Bonding Interaction Regulates Photoisomerization of a Single-Bond-Rotation Locked Photoactive Yellow Protein Chromophore in Protein. *J. Phys. Chem. Lett.* **2020**, *11*, 2470−2476.
(21) Kundu, S.; Makri, N. Modular Path Integral for Finite-Temperature Dynamics of Extended Systems with Intramolecular Vibrations. *J. Chem. Phys.* **2020**, *153*, 044124.
(22) Kundu, S.; Makri, N. Real-Time Path Integral Simulation of Exciton-Vibration Dynamics in Light-Harvesting Bacteriochlorophyll Aggregates. *J. Phys. Chem. Lett.* **2020**, *11*, 8783−8789.
(23) Tanimura, Y. Numerically "Exact" Approach to Open Quantum Dynamics: The Hierarchical Equations of Motion (HEOM). *J. Chem. Phys.* **2020**, *153*, 020901.
(24) Yan, Y.; Xing, T.; Shi, Q. A New Method to Improve the Numerical Stability of the Hierarchical Equations of Motion for Discrete Harmonic Oscillator Modes. *J. Chem. Phys.* **2020**, *153*, 204109.
(25) Wang, H.; Thoss, M. Multilayer Formulation of the Multiconfiguration Time-Dependent Hartree Theory. *J. Chem. Phys.* **2003**, *119*, 1289−12.
(26) Meyer, H.-D.; Gatti, F.; Worth, G. A. *Multidimensional Quantum Dynamics: MCTDH Theory and Applications*; Wiley-VCH: Weinheim, Germany, 2009.
(27) Wang, H.; Thoss, M. A Multilayer Multiconfiguration Time-Dependent Hartree Simulation of the Reaction-Coordinate Spin-Boson Model Employing an Interaction Picture. *J. Chem. Phys.* **2017**, *146*, 124112.
(28) Ren, J.; Shuai, Z.; Kin-Lic Chan, G. Time-Dependent Density Matrix Renormalization Group Algorithms for Nearly Exact Absorption and Fluorescence Spectra of Molecular Aggregates at Both Zero and Finite Temperature. *J. Chem. Theory Comput.* **2018**, *14*, 5027−5039.
(29) Baiardi, A.; Reiher, M. Large-Scale Quantum Dynamics with Matrix Product States. *J. Chem. Theory Comput.* **2019**, *15*, 3481−3498.
(30) Li, W.; Ren, J.; Shuai, Z. Finite-Temperature TD-DMRG for the Carrier Mobility of Organic Semiconductors. *J. Phys. Chem. Lett.* **2020**, *11*, 4930−4936.
(31) Gelin, M. F.; Borrelli, R. Simulation of Nonlinear Femtosecond Signals at Finite Temperature via a Thermo Field Dynamics-Tensor Train Method: General Theory and Application to Time- and Frequency-Resolved Fluorescence of the Fenna−Matthews−Olson Complex. *J. Chem. Theory Comput.* **2021**, *17*, 4316−4331.
(32) Lyu, N.; Mulvihill, E.; Soley, M. B.; Geva, E.; Batista, V. S. Tensor-Train Thermo-Field Memory Kernels for Generalized Quantum Master Equations. *J. Chem. Theory Comput.* **2023**, *19*, 1111−1129.
(33) Cotton, S. J.; Miller, W. H. Symmetrical Windowing for Quantum States in Quasi-Classical Trajectory Simulations: Application to Electronically Non-Adiabatic Processes. *J. Chem. Phys.* **2013**, *139*, 234112.
(34) Cotton, S. J.; Igumenshchev, K.; Miller, W. H. Symmetrical Windowing for Quantum States in Quasi-Classical Trajectory Simulations: Application to Electron Transfer. *J. Chem. Phys.* **2014**, *141*, 084104.
(35) Cotton, S. J.; Miller, W. H. A New Symmetrical Quasi-Classical Model for Electronically Non-Adiabatic Processes: Application to the Case of Weak Non-Adiabatic Coupling. *J. Chem. Phys.* **2016**, *145*, 144108.
(36) Cotton, S. J.; Miller, W. H. A Symmetrical Quasi-Classical Windowing Model for the Molecular Dynamics Treatment of Non-Adiabatic Processes Involving Many Electronic States. *J. Chem. Phys.* **2019**, *150*, 104101.
(37) Sun, X.; Miller, W. H. Semiclassical Initial Value Representation for Electronically Nonadiabatic Molecular Dynamics. *J. Chem. Phys.* **1997**, *106*, 6346−6353.
(38) Gao, X.; Saller, M. A. C.; Liu, Y.; Kelly, A.; Richardson, J. O.; Geva, E. Benchmarking Quasiclassical Mapping Hamiltonian Methods for Simulating Electronically Nonadiabatic Molecular Dynamics. *J. Chem. Theory Comput.* **2020**, *16*, 2883−2895.
(39) Saller, M. A. C.; Kelly, A.; Richardson, J. O. On the Identity of the Identity Operator in Nonadiabatic Linearized Semiclassical Dynamics. *J. Chem. Phys.* **2019**, *150*, 071101.
(40) Ishizaki, A.; Fleming, G. R. Theoretical Examination of Quantum Coherence in a Photosynthetic System at Physiological Temperature. *Proc. Natl. Acad. Sci. U.S.A.* **2009**, *106*, 17255−17260.
(41) Adolphs, J.; Renger, T. How Proteins Trigger Excitation Energy Transfer in the FMO Complex of Green Sulfur Bacteria. *Biophys. J.* **2006**, *91*, 2778−2797.
(42) Moix, J.; Wu, J.; Huo, P.; Coker, D.; Cao, J. Efficient Energy Transfer in Light-Harvesting Systems, III: The Influence of the Eighth Bacteriochlorophyll on the Dynamics and Efficiency in FMO. *J. Phys. Chem. Lett.* **2011**, *2*, 3045−3052.
(43) Oh, S. A.; Coker, D. F.; Hutchinson, D. A. W. Optimization of Energy Transport in the Fenna−Matthews−Olson Complex via Site-Varying Pigment−Protein Interactions. *J. Chem. Phys.* **2019**, *150*, 085102.
(44) Jia, X.; Mei, Y.; Zhang, J. Z.; Mo, Y. Hybrid QM/MM Study of FMO Complex with Polarized Protein-Specific Charge. *Sci. Rep.* **2015**, *5*, 17096.
(45) Huai, Z.; Tong, Z.; Mei, Y.; Mo, Y. Theoretical Study of the Spectral Differences of the Fenna−Matthews−Olson Protein from Different Species and Their Mutants. *J. Phys. Chem. B* **2021**, *125*, 8313−8324.
(46) Walters, P. L.; Allen, T. C.; Makri, N. Direct Determination of Discrete Harmonic Bath Parameters from Molecular Dynamics Simulations. *J. Comput. Chem.* **2017**, *38*, 110−115.
(47) Tong, Z.; Gao, X.; Cheung, M. S.; Dunietz, B. D.; Geva, E.; Sun, X. Charge Transfer Rate Constants for the Carotenoid−Porphyrin−C_{60} Molecular Triad Dissolved in Tetrahydrofuran: The

https://doi.org/10.1021/acs.jctc.3c00770
J. Chem. Theory Comput. 2023, 19, 7151−7170

Spin-Boson Model vs the Linearized Semiclassical Approximation. *J. Chem. Phys.* **2020**, *153*, 044105.
(48) Weiss, U. *Quantum Dissipative Systems*; World Scientific: Singapore, 2012.
(49) Xu, D.; Schulten, K. Coupling of Protein Motion to Electron Transfer in a Photosynthetic Reaction Center: Investigating the Low Temperature Behavior in the Framework of the Spin-Boson Model. *Chem. Phys.* **1994**, *182*, 91−117.
(50) Sun, X.; Geva, E. Equilibrium Fermi's Golden Rule Charge Transfer Rate Constants in the Condensed Phase: The Linearized Semiclassical Method vs Classical Marcus Theory. *J. Phys. Chem. A* **2016**, *120*, 2976−2990.
(51) Cho, M.; Silbey, R. J. Nonequilibrium Photoinduced Electron Transfer. *J. Chem. Phys.* **1995**, *103*, 595−606.
(52) Brian, D.; Liu, Z.; Dunietz, B. D.; Geva, E.; Sun, X. Three-State Harmonic Models for Photoinduced Charge Transfer. *J. Chem. Phys.* **2021**, *154*, 174105.
(53) Hu, Z.; Brian, D.; Sun, X. Multi-State Harmonic Models with Globally Shared Bath for Nonadiabatic Dynamics in the Condensed Phase. *J. Chem. Phys.* **2021**, *155*, 124105.
(54) Hu, Z.; Sun, X. All-Atom Nonadiabatic Semiclassical Mapping Dynamics for Photoinduced Charge Transfer of Organic Photovoltaic Molecules in Explicit Solvents. *J. Chem. Theory Comput.* **2022**, *18*, 5819−5836.
(55) Hu, Z.; Liu, Z.; Sun, X. Effects of Heterogeneous Protein Environment on Excitation Energy Transfer Dynamics in the Fenna-Matthews-Olson Complex. *J. Phys. Chem. B* **2022**, *126*, 9271−9287.
(56) Caldeira, A. O.; Leggett, A. J. Quantum Tunnelling in a Dissipative System. *Ann. Phys.* **1983**, *149*, 374−456.
(57) Leggett, A. J. Quantum Tunneling in the Presence of an Arbitrary Linear Dissipation Mechanism. *Phys. Rev. B* **1984**, *30*, 1208−1218.
(58) Leggett, A. J.; Chakravarty, S.; Dorsey, A. T.; Fisher, M. P. A.; Garg, A.; Zwerger, W. Dynamics of the Dissipative Two-State System. *Rev. Mod. Phys.* **1987**, *59*, 1−85.
(59) Garg, A.; Onuchic, J. N.; Ambegaokar, V. Effect of Friction on Electron Transfer in Biomolecules. *J. Chem. Phys.* **1985**, *83*, 4491−4503.
(60) Cederbaum, L. S.; Gindensperger, E.; Burghardt, I. Short-Time Dynamics Through Conical Intersections in Macrosystems. *Phys. Rev. Lett.* **2005**, *94*, 113003.
(61) Hughes, K. H.; Christ, C. D.; Burghardt, I. Effective-Mode Representation of Non-Markovian Dynamics: A Hierarchical Approximation of the Spectral Density. I. Application to Single Surface Dynamics. *J. Chem. Phys.* **2009**, *131*, 024109.
(62) Hughes, K. H.; Christ, C. D.; Burghardt, I. Effective-Mode Representation of Non-Markovian Dynamics: A Hierarchical Approximation of the Spectral Density. II. Application to Environment-Induced Nonadiabatic Dynamics. *J. Chem. Phys.* **2009**, *131*, 124108.
(63) Popp, W.; Polkehn, M.; Hughes, K. H.; Martinazzo, R.; Burghardt, I. Vibronic Coupling Models for Donor-Acceptor Aggregates Using an Effective-Mode Scheme: Application To Mixed Frenkel And Charge-Transfer Excitons in Oligothiophene Aggregates. *J. Chem. Phys.* **2019**, *150*, 244114.
(64) Popp, W.; Polkehn, M.; Binder, R.; Burghardt, I. Coherent Charge Transfer Exciton Formation in Regioregular P3HT: A Quantum Dynamical Study. *J. Phys. Chem. Lett.* **2019**, *10*, 3326−3332.
(65) Popp, W.; Brey, D.; Binder, R.; Burghardt, I. Quantum Dynamics of Exciton Transport and Dissociation in Multichromophoric Systems. *Annu. Rev. Phys. Chem.* **2021**, *72*, 591−616.
(66) Makri, N. Topological Aspects of System-Bath Hamiltonians and a Vector Model for Multisite Systems Coupled to Local, Correlated, or Common Baths. *J. Chem. Phys.* **2023**, *158*, 144107.
(67) Liddell, P. A.; Kuciauskas, D.; Sumida, J. P.; Nash, B.; Nguyen, D.; Moore, A. L.; Moore, T. A.; Gust, D. Photoinduced Charge Separation and Charge Recombination to a Triplet State in a Carotene−Porphyrin−Fullerene Triad. *J. Am. Chem. Soc.* **1997**, *119*, 1400−1405.
(68) Liddell, P. A.; Kodis, G.; Moore, A. L.; Moore, T. A.; Gust, D. Photonic Switching of Photoinduced Electron Transfer in a Dithienylethene−Porphyrin−Fullerene Triad Molecule. *J. Am. Chem. Soc.* **2002**, *124*, 7668−7669.
(69) Kuciauskas, D.; Liddell, P. A.; Lin, S.; Stone, S. G.; Moore, A. L.; Moore, T. A.; Gust, D. Photoinduced Electron Transfer in Carotenoporphyrin−Fullerene Triads: Temperature and Solvent Effects. *J. Phys. Chem. B* **2000**, *104*, 4307−4321.
(70) Andrea Rozzi, C.; Maria Falke, S.; Spallanzani, N.; Rubio, A.; Molinari, E.; Brida, D.; Maiuri, M.; Cerullo, G.; Schramm, H.; Christoffers, J.; Lienau, C. Quantum Coherence Controls the Charge Separation in a Prototypical Artificial Light−Harvesting System. *Nat. Commun.* **2013**, *4*, 1602−1607.
(71) Hu, Z.; Tong, Z.; Cheung, M. S.; Dunietz, B. D.; Geva, E.; Sun, X. Photoinduced Charge Transfer Dynamics in the Carotenoid−Porphyrin−C_{60} Triad via the Linearized Semiclassical Nonequilibrium Fermi's Golden Rule. *J. Phys. Chem. B* **2020**, *124*, 9579−9591.
(72) Engel, G. S.; Calhoun, T. R.; Read, E. L.; Ahn, T.-K.; Mančal, T.; Cheng, Y.-C.; Blankenship, R. E.; Fleming, G. R. Evidence for Wavelike Energy Transfer through Quantum Coherence in Photosynthetic Systems. *Nature* **2007**, *446*, 782−786.
(73) Duan, H.-G.; Prokhorenko, V. I.; Cogdell, R. J.; Ashraf, K.; Stevens, A. L.; Thorwart, M.; Miller, R. J. D. Nature Does Not Rely on Long-Lived Electronic Quantum Coherence for Photosynthetic Energy Transfer. *Proc. Natl. Acad. Sci. U.S.A.* **2017**, *114*, 8493−8498.
(74) Thyrhaug, E.; Tempelaar, R.; Alcocer, M. J.; Žídek, K.; Bína, D.; Knoester, J.; Jansen, T. L. C.; Zigmantas, D. Identification and Characterization of Diverse Coherences in the Fenna−Matthews−Olson Complex. *Nat. Chem.* **2018**, *10*, 780−786.
(75) Rolczynski, B. S.; Zheng, H.; Singh, V. P.; Navotnaya, P.; Ginzburg, A. R.; Caram, J. R.; Ashraf, K.; Gardiner, A. T.; Yeh, S.-H.; Kais, S.; et al. Correlated Protein Environments Drive Quantum Coherence Lifetimes in Photosynthetic Pigment-Protein Complexes. *Chem.* **2018**, *4*, 138−149.
(76) Maiuri, M.; Ostroumov, E. E.; Saer, R. G.; Blankenship, R. E.; Scholes, G. D. Coherent Wavepackets in the Fenna−Matthews−Olson Complex Are Robust to Excitonic-Structure Perturbations Caused by Mutagenesis. *Nat. Chem.* **2018**, *10*, 177−183.
(77) Sun, X.; Geva, E. Exact vs. Asymptotic Spectral Densities in the Garg-Onuchic-Ambegaokar Charge Transfer Model and its Effect on Fermi's Golden Rule Rate Constants. *J. Chem. Phys.* **2016**, *144*, 044106.
(78) Sun, X.; Geva, E. Nonequilibrium Fermi's Golden Rule Charge Transfer Rates via the Linearized Semiclassical Method. *J. Chem. Theory Comput.* **2016**, *12*, 2926−2941.
(79) Voityuk, A. A.; Rösch, N. Fragment Charge Difference Method for Estimating Donor−Acceptor Electronic Coupling: Application to DNA π-Stacks. *J. Chem. Phys.* **2002**, *117*, 5607−5616.
(80) Householder, A. S. Unitary Triangularization of a Nonsymmetric Matrix. *J. ACM* **1958**, *5*, 339−342.
(81) Brian, D.; Sun, X. Charge-Transfer Landscape Manifesting the Structure-Rate Relationship in the Condensed Phase via Machine Learning. *J. Phys. Chem. B* **2021**, *125*, 13267−13278.
(82) Case, D. A.; Ben-Shalom, I. Y.; Brozell, S. R.; Cerutti, D. S.; Cheatham, T. E.; Cruzeiro, V. W. D.; Darden, T. A.; Duke, R. E.; Ghoreishi, D.; Gilson, M. K. et al. *AMBER 2020*; University of California: San Francisco, 2020.
(83) Darden, T.; York, D.; Pedersen, L. Particle Mesh Ewald: An Nlog(N) Method for Ewald Sums in Large Systems. *J. Chem. Phys.* **1993**, *98*, 10089−10092.
(84) Ciccotti, G.; Ryckaert, J. P. Molecular Dynamics Simulation of Rigid Molecules. *Comput. Phys. Rep.* **1986**, *4*, 346−392.
(85) Wang, J.; Wolf, R. M.; Caldwell, J. W.; Kollman, P. A.; Case, D. A. Development and Testing of a General Amber Force Field. *J. Comput. Chem.* **2004**, *25*, 1157−1174.
(86) Sun, X.; Zhang, P.; Lai, Y.; Williams, K. L.; Cheung, M. S.; Dunietz, B. D.; Geva, E. Computational Study of Charge-Transfer Dynamics in the Carotenoid−Porphyrin−C_{60} Molecular Triad

https://doi.org/10.1021/acs.jctc.3c00770
J. Chem. Theory Comput. 2023, 19, 7151−7170

Solvated in Explicit Tetrahydrofuran and Its Spectroscopic Signature. *J. Phys. Chem. C* **2018**, *122*, 11288−11299.
(87) Shao, Y.; Gan, Z.; Epifanovsky, E.; Gilbert, A. T.; Wormit, M.; Kussmann, J.; Lange, A. W.; Behn, A.; Deng, J.; Feng, X.; et al. Advances in Molecular Quantum Chemistry Contained in the Q-Chem 4 Program Package. *Mol. Phys.* **2015**, *113*, 184−215.
(88) Ehrenfest, P. Comment on the Approximate Validity of Classical Mechanics within Quantum Mechanics. *Z. Phys.* **1927**, *45*, 455−457.
(89) Runeson, J. E.; Richardson, J. O. Generalized Spin Mapping for Quantum-Classical Dynamics. *J. Chem. Phys.* **2020**, *152*, 084110.
(90) Meyer, H.-D.; Miller, W. H. A Classical Analog for Electronic Degrees of Freedom in Nonadiabatic Collision Processes. *J. Chem. Phys.* **1979**, *70*, 3214−3223.
(91) Stock, G.; Thoss, M. Semiclassical Description of Nonadiabatic Quantum Dynamics. *Phys. Rev. Lett.* **1997**, *78*, 578−581.
(92) Sun, X.; Geva, E. Non-Condon Nonequilibrium Fermi's Golden Rule Rates from the Linearized Semiclassical Method. *J. Chem. Phys.* **2016**, *145*, 064109.
(93) Shi, Q.; Geva, E. A New Approach to Calculating the Memory Kernel of the Generalized Quantum Master Equation for an Arbitrary System-Bath Coupling. *J. Chem. Phys.* **2003**, *119*, 12063.
(94) Brian, D.; Sun, X. Generalized Quantum Master Equation: A Tutorial Review and Recent Advances. *Chin. J. Chem. Phys.* **2021**, *34*, 497−524.
(95) Mulvihill, E.; Geva, E. A Road Map to Various Pathways for Calculating the Memory Kernel of the Generalized Quantum Master Equation. *J. Phys. Chem. B* **2021**, *125*, 9834−9852.
(96) Chaudhuri, S.; Hedström, S.; Méndez-Hernández, D. D.; Hendrickson, H. P.; Jung, K. A.; Ho, J.; Batista, V. S. Electron Transfer Assisted by Vibronic Coupling from Multiple Modes. *J. Chem. Theory Comput.* **2017**, *13*, 6000−6009.
(97) Biasin, E.; Fox, Z. W.; Andersen, A.; Ledbetter, K.; Kjær, K. S.; Alonso-Mori, R.; Carlstad, J. M.; Chollet, M.; Gaynor, J. D.; Glownia, J. M.; Hong, K.; Kroll, T.; Lee, J. H.; Liekhus-Schmaltz, C.; Reinhard, M.; Sokaras, D.; Zhang, Y.; Doumy, G.; March, A. M.; Southworth, S. H.; Mukamel, S.; Gaffney, K. J.; Schoenlein, R. W.; Govind, N.; Cordones, A. A.; Khalil, M. Direct Observation of Coherent Femtosecond Solvent Reorganization Coupled to Intramolecular Electron Transfer. *Nat. Chem.* **2021**, *13*, 343−349.
(98) Özdemir, A. D.; Inanlou, S.; Symalla, F.; Xie, W.; Wenzel, W.; Elstner, M. Dynamic Effects on Hole Transport in Amorphous Organic Semiconductors: a Combined QM/MM and kMC Study. *J. Chem. Theory Comput.* **2023**, *19*, 3849−3860.

https://doi.org/10.1021/acs.jctc.3c00770
J. Chem. Theory Comput. 2023, 19, 7151−7170